A&A 473, 149–162 (2007)
DOI: 10.1051/0004-6361:20077733

Astronomy
&
Astrophysics

A close look at the heart of RCW 108[⋆,⋆⋆]

F. Comerón[1] and N. Schneider[2]

[1] ESO, Karl-Schwarzschild-Str. 2, 85748 Garching bei München, Germany
e-mail: `fcomeron@eso.org`
[2] SAp/CEA Saclay, 91191 Gif-sur-Yvette, France
e-mail: `nschneid@cea.fr`

Received 27 April 2007 / Accepted 4 July 2007

ABSTRACT

Context. The IRAS 16362-4845 star-forming site in the RCW 108 complex contains an embedded compact cluster that includes some massive O-type stars. Star formation in the complex, and in particular in IRAS 16362-4845, has been proposed to be externally triggered by the action of NGC 6193.

Aims. We present a photometric study of the IRAS 16362-4845 cluster sensitive enough to probe the massive brown dwarf regime. In particular, we try to verify an apparent scarcity of solar-type and low-mass stars reported in a previous paper (Comerón et al. 2005, A&A, 433, 955).

Methods. Using NACO at the VLT we have carried out adaptive optics-assisted imaging in the JHK_SL' bands, as well as through narrow-band filters centered on the Brγ and the H_2 $S(1)$ $v = 1 \rightarrow 0$ lines. We estimate individual line-of-sight extinctions and, for stars detected in the three JHK_S filters, we estimate the contribution to the K_S flux caused by light reprocessed in the circumstellar environment. We also resolve close binary and multiple systems. We use the K luminosity function as a diagnostic tool for the characteristics of the underlying mass function.

Results. IRAS 16362-4845 does contain young low-mass stars. Nevertheless, they are far less than those expected from the extrapolation of the bright end of the K luminosity function towards fainter magnitudes. We estimate a total stellar mass of 370 $M_\odot$. Nearly all the cluster members display L' excesses, whereas K_S excesses are in general either absent or moderate (<1 mag). We also detect an extremely red object with $(K_S - L') > 9$, likely to be a Class I source.

Conclusions. The fact that solar-type and low-mass stars are present in numbers much smaller than those expected from the number of more massive members hints at an initial mass function deficient in low mass stars as compared to that of other young clusters such as the Trapezium. The origin of this difference is unclear, and we speculate that it might be due to external triggering having started star formation in the cluster, perhaps producing a top-heavy initial mass function. We also note that there are no detectable systematic differences between the spatial distributions of bright and faint cluster members. Such absence of mass segregation in the spatial distribution of stars may also support external triggering having played an important role in the history of the RCW 108 region.

Key words. ISM: HII regions – ISM: individual objects: RCW 108 – stars: luminosity function, mass function – open clusters and associations: IRAS 16362-4845

1. Introduction

The RCW 108 HII region in the Ara OB1 association has long been regarded as one of the best case studies illustrating the eroding action of newly formed clusters containing massive stars on the molecular gas in their environments (Shaver & Goss 1970; Straw et al. 1987; Comerón et al. 2005). In visible-light images of the region (see e.g. Petersen 2001) RCW 108 appears as a bright rim nebula (SFO 79 in the catalog of Sugitani et al. 1991) on a size scale of several 10 arcmin, defining a sharp boundary between an extended molecular cloud in the west and a region predominantely filled with ionized gas in the east. The rim represents the ionization front, produced when the ultraviolet radiation from O-type stars of the neighboring cluster NGC 6193 hit and progressively destroy the molecular cloud.

Infrared sources indicating active star forming sites are common among externally ionized molecular clouds (Sugitani et al. 1989, 1991, 1995; Sugitani & Ogura 1994), which has been interpreted as evidence for star formation triggered by radiation-driven implosion of dense cores (e.g. Bertoldi 1989; Miao et al. 2006). This mechanism may well be at work in RCW 108, as noted by the indications of triggered star formation in the region recently discussed by Urquhart et al. (2004) and Comerón et al. (2005, hereafter CSR05).

The most conspicuous star forming site in RCW 108 is the compact HII region IRAS 16362-4845, first noted by Shaver & Goss (1970). It is deeply embedded in the dense molecular cloud and associated with a cluster of IR-sources discovered by Straw et al. (1987). Its stellar contents has been more recently studied by Urquhart et al. (2004), based on the 2MASS catalog (Skrutskie et al. 2006); by CSR05 by means of dedicated deeper, higher resolution JHK_S imaging; and by Wolk et al. (2007) using X-ray emission as a tracer of young stellar populations. The study of CSR05 indicates that the IRAS 16362-4845 embedded aggregate is a Trapezium-like cluster containing at least one late O-type star, in consistency with the visible spectrum of the heavily obscured HII region. The mass of the cluster was estimated by CSR05 to be ~210 $M_\odot$, with a rather large uncertainty. Furthermore, that study noted as an intriguing feature of the color–magnitude diagram an apparent lack of stars fainter than $M_K \simeq +1.0$ and with amounts of foreground reddening

---

[⋆] Based on observations obtained at the European Southern Observatory using the Very Large Telescope (VLT) (programme 077.C-0660(A)), on Cerro Paranal, Chile.

[⋆⋆] Table 2 is only available in electronic form at `http://www.aanda.org` in the range covered by the brightest stars in the cluster, which might be indicative of a peculiar mass function.

While the result hinted at by CSR05 may be potentially relevant to understand the build-up of the initial mass function (IMF) in clusters dominated by massive stars, some practical limitations of the observations presented in that work advised a further analysis based on material of higher quality. First and foremost, though the observations were deep enough to penetrate well into the area of the color–magnitude diagram where the lack of the stars was noted, the completeness of the census in that range was difficult to assess. This was due to the presence of bright nebulosity pervading the cluster with large brightness variations over small angular scales. Secondly, although the observed stellar images have a full-width at half maximum (FWHM) below one arcsecond, the combination of crowdedness and nebulosity still hampered the detection of faint members relatively close to brighter stars. For these reasons, higher quality observations were needed to place our tentative conclusion of a deficit of faint members in IRAS 16362-4845 on a firm standing.

In this paper, we present new observations of the IRAS 16362-4845 cluster carried out using adaptive optics near-infrared imaging at the Very Large Telescope (VLT), which provide a far deeper and sharper view of the cluster than previously available. This new material allows us to reassess the stellar contents of the cluster, and address questions related to possible peculiarities of its IMF, the frequency of infrared excesses among its members, the abundance of massive binary stars, or the spatial distribution of high- and low-mass members, also providing some further insights on the structure of the associated nebula.

2. Observations

2.1. Data acquisition and reduction

Our observations were carried out in service mode using NACO, the adaptive optics near-infrared camera and spectrograph at the VLT (Rousset et al. 2002, Lenzen et al. 2003), in imaging mode. Broad-band images were obtained through the J (1.26 μm), H (1.66 μm), K_S (2.18 μm), and L' (3.80 μm) filters, as well as through two narrow-band filters centered on 2.12 μm and 2.17 μm respectively sampling the nebular emission in the $\mathrm{H}_2\,S(1)\;v=1\rightarrow 0$ and Brγ lines. The brightest star in the field in K_S-band images of the cluster, star #12 from CSR05 (hereafter CSR-012A[1]) has $K_\mathrm{S}=8.36$ and was used for wavefront sensing, using the near-infrared wavefront sensor in NAOS, the adaptive optics module of NACO. Different available dichroics were chosen, depending on the band of the observations: the K dichroic for the J and H observations (90% transmitted light in those bands), the JHK dichroic for the L' observations (also 90% transmission in that band), and the N20C80 dichroic for the K_S, 2.12 μm, and 2.17 μm observations (80% transmission). These choices provide the best compromises between the signal from the wavefront reference star needed for a good adaptive optics correction and the light transmitted to CONICA, the camera of NACO. We selected the wide-field camera optics yielding a pixel scale of 54 milliarcseconds per pixel for the images in the J, H, and K_S bands and the narrow-band. The resulting field size, $54''$, matches well the angular size of the IRAS 16362-4845 cluster ($\sim 30''$), whereas the location of CSR-012A near the northern border of the cluster allows us to sample a portion of the dark cloud located to the north of IRAS 16362-4845. For the L' band observations the maximum field size of the field attainable with NACO is $27''$, at a scale of 27 milliarcseconds per pixel. Our observations through that filter thus sample only the densest part of the cluster centered on CSR-012A.

Table 1. Log of observations.

Filter	*DIT*	*NDIT*	*NEXP*	Date
J	13 s	5	16	29/30 June 2006
				29/30 June 2006
H	20 s	4	16	27/28 July 2006
K_S	20 s	4	16	22/23 July 2006
				24/25 July 2006
L'	0.175 s	180	28	29/30 June 2006
				29/30 June 2006
2.17	65	1	16	22/23 July 2006
				22/23 July 2006
2.12	65	1	16	17/18 July 2006
				28/29 July 2006

The observations were obtained on six different nights between 29/30 June and and 28/29 July 2006. The images were performed through two series of exposures in each of the J, K_S, L', 2.12 μm, and 2.17 μm filters, and one series of exposures in the H filter. We used the common technique of stacking a number *NDIT* of frames, each with a detector integration time *DIT*, centered on a number *NEXP* of closely spaced telescope pointings on a random dither pattern, for which we used an amplitude of $10''$. The image resulting from each exposure was constructed by combining the sky-subtracted individual stacks after correcting for the telescope offset between pointings. This procedure was also used for the L' band observations, rather than the alternative chop-and-nod technique. Table 1 gives the log of the observations, including the individual exposure parameters. Sky subtraction from our on-target images was performed by stacking intercalated images obtained around a separate sky position located $3'$ away from IRAS 16362-4845, as the bright nebulosity pervading the cluster prevented us from using for that purpose the median-filtered on-target frames uncorrected for telescope offsets, as is normally done on uncrowded, nebulosity-free fields. The detector readout mode was selected for each filter as the best compromise between the necessary sensitivity and the dynamic range available. For the filters in which two images were obtained on separate observations, one combined frame was produced and used for further analysis. Figure 1 shows a composite of the final frames obtained through the JHK_S filters.

2.2. Photometry

Our observations in the JHK_S bands were calibrated using the infrared photometry of non-saturated sources in common with those listed in CSR05. The L' photometry was calibrated using as a reference the stars in the field observed in that same band by Straw et al. (1987).

The intrinsic difficulty of performing stellar photometry in observations using adaptive optics, due to the noticeable variation of the point-spread function (PSF) across the field, is compounded in our case with the additional complication of a variable nebular background pervading the area of the cluster, which makes it difficult to accurately estimate the contribution to the

---

[1] We use the nomenclature CSR-*nnn* to refer to the stars listed in Table 2 of CSR05. Stars detected in the present work and not listed in CSR05 are named CS-*nnn*. Members of multiple systems are referred to by adding A, B,... to their numbers. In this way, CSR-012A is the brightest member of the system collectively identified as Star #12 in CSR05, which the current observations show to be composed of five members.

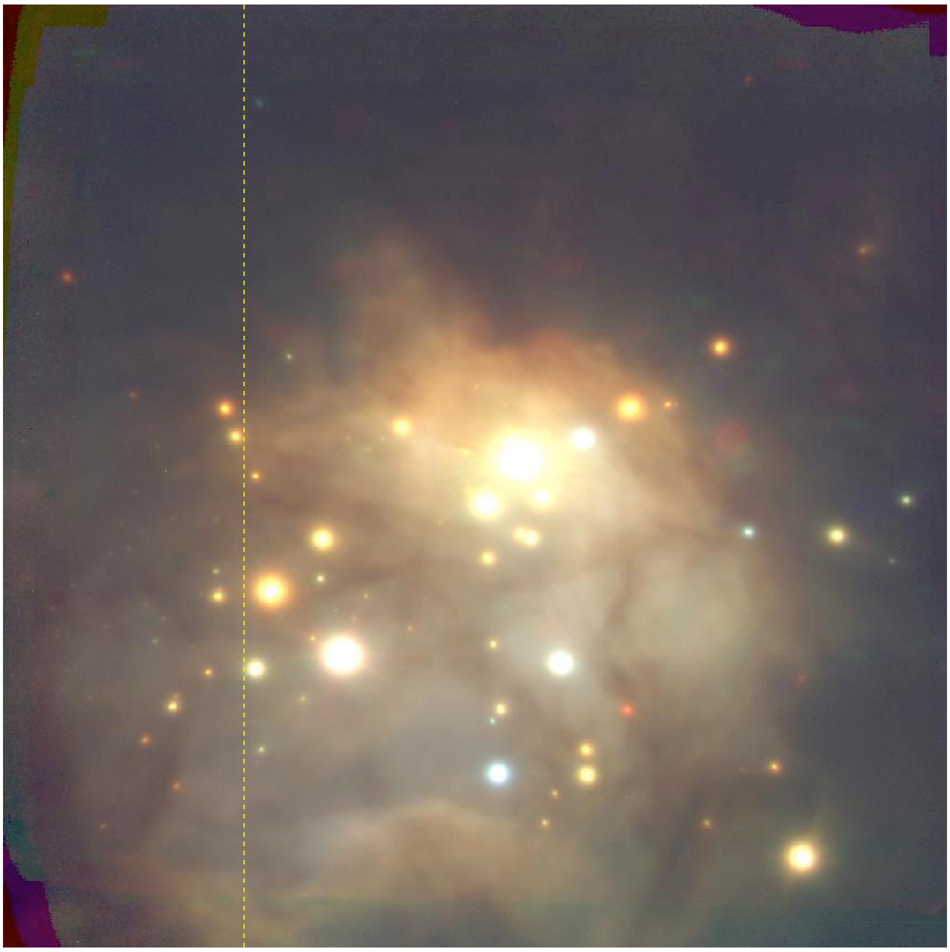

Fig. 1. A color composite of the frames of IRAS 16362-4845 obtained through the J (blue), H (green) and K_S (red) filters. The frames are centered on the brightest source at near-infrared wavelengths, CSR-012A ($\alpha(2000) = 16^h40^m00^s\!.2$, $\delta(2000) = -48°51'40''$). The field covered is $52'' \times 57''$, with North at the top and East to the left. A comparison with Fig. 12 of CSR05 gives an appreciation of the increase in quality between the observations discussed in that paper and those presented here. The small red ring just outside the upper right edge of the nebula is actually an artifact due to out-of-focus ghosts of the brightest star in the cluster. The dashed line corresponds to $\alpha(2000) = 16^h40^m01^s\!.78$. As explained in Sect. 3.2 contamination by background sources is higher to the East of this line, and we exclude that region from our analysis.

measurement of the extended wings of the PSF. The strong and complicated variation of the PSF, particularly in the J band where the adaptive optics correction is poorer and degrades fastest with the distance to the wavefront reference star, led us not to consider PSF fitting as a suitable method. Instead, we obtained better results by performing aperture photometry at the position of each detected object. Source detection was carried out automatically using the DAOFIND task in the DAOPHOT package layered on IRAF[2] (Stetson 1987). The choice of parameters of the task, in particular the sharpness and roundness cutoff parameters, was made by successive trials by comparing the results of the automatic detection with a careful visual inspection of the frames. We identified the sources that were left undetected by DAOFIND as well as the false detections, relying on the fact that the human eye ultimately provides the best discriminant between real stellar sources and detection artifacts.

The radius of the aperture for photometry was chosen as five times the FWHM of the PSF of a bright, non-saturated star located 15″ away from the wavefront reference star, which provided an average PSF of the field. We verified that the relatively large number by which the FWHM of the PSF of that star was multiplied ensured a negligible aperture correction elsewehere in the field. The counts within this aperture were computed by dividing the aperture into concentric rings each with a width of one pixel. Pixel values deviating by more than 3σ from the average value within each ring normally denoted the existence of a close companion to the star being measured, and were thus replaced by the average of the other pixels of the ring. For some faint stars located in regions of a strongly variable background this procedure prevented us from obtaining reliable magnitude measurements. Table 2 gives the photometric measurements obtained for all the stars in our images, and is available in full electronically.

2.3. Completeness limits

The magnitude completeness limits of our observations are not straightforward to assess due to the same factors that complicated the photometric measurements. On average the better adaptive optics correction obtained near the wavefront reference star, which leads in principle to deeper detection limits, is partly offset by the fact that this star lies near the peak of the surface brightness of the nebula. In the H and K_S band images, where the adaptive optics correction is best and improves image quality over a larger field, the deepest detection limits are actually obtained near the edges of the frames, where stellar images are

---

[2] IRAF is distributed by NOAO, which is operated by the Association of Universities for Research in Astronomy, Inc., under contract to the National Science Foundation.

Table 3. Completeness and detection limits.

Filter	Completeness	Detection
J	18.6	21.2
H	19.1	21.5
K_S	18.0	20.6
L'	13.5	14.1

not as sharp as near the centers but the background nebulosity is nearly absent.

Since knowledge of the completeness of the stellar census of the cluster is of great importance for the ensuing discussions on the luminosity function of the cluster, we performed numerical simulations on the reduced frames using artificial stars. To this end, stars at different positions of the field were used as local PSF references, and artificial stars of various magnitudes and the same PSF were added within a radius of $10''$ from each local PSF reference. The same detection procedure and parameters used for the detection of the real sources were then applied to the image containing the artificial stars. The completeness limit was then adopted as the magnitude of the artificial stars for which at least 95% of them were recovered by DAOFIND in the surroundings of any of the local PSF reference stars used to define them. The location of such reference stars in all representative regions in terms of nebular brightness and adaptive optics corrections ensures that any star brighter than the completeness limit thus defined (except those in the close proximity of the brightest stars) are indeed detected and incorporated to our census of members of the IRAS16362-4845 cluster. Nevertheless, it was found, as expected, that many regions of the cluster provided considerably deeper detection limits, and our census thus contains numerous stars below the completeness threshold. Table 3 lists both the completeness and 5σ detection limits, taking into account that the latter apply only to limited areas of the region imaged and are generally brighter elsewhere where the nebulosity is more intense.

3. Results

3.1. Overall structure of the cluster and its nebula

Figure 1 presents an overall view of the structure of the cluster and the associated nebulosity, and Fig. 2 gives a more detailed view of the nebula through the narrow-band filters centered on the line emission of Brγ and H_2. At near-infrared wavelengths the cluster is dominated by the likely O-type star CSR-012A (=IRS29, in Straw et al. 1987), near the Northern edge of the HII region. Our new observations reveal it to be a tight concentration of five stars within $1\farcs1$ of the primary (Fig. 3). As already noted by Straw et al. two other stars to the East of the cluster, CSR-18 and CSR-20 (=IRS19 and IRS20, in Straw et al.), become dominant in the L' band, and other bright members appear elsewhere in the cluster. The close correspondence between the cluster and the bright nebulosity is well apparent from Fig. 1, although some cluster members appear projected beyond the boundaries of the nebula. The approximate diameter of the cluster is $40''$, corresponding to 0.25 pc at the distance of 1.3 kpc (distance modulus 10.6) that we adopt in this paper (see Arnal et al. 2003).

The appearance of the nebulosity is reminiscent of a cocoon surrounding most of the stars, except towards the East where the nebulosity fades away without a border as well defined as towards the other directions. This is well seen in Fig. 2, where the H_2 nebulosity wisps tracing the edges of photodissociation regions at the interface between the molecular cloud and the HII region are absent towards the East, and where the Brγ also brightens near the Western edge. The edge is actually the brightest feature of the HII region at longer wavelengths, as shown by the image obtained with the Spitzer Space Observatory using the IRAC camera at 8 μm, available from the Spitzer archive, where emission is dominated by PAH molecules (see Fig. 4). The overall morphology of the nebula may be due to the overpressure of the cluster gas originated by its ionization having been released by an outflow towards the East. Both the molecular-line and the Hα observations presented in CSR05 support this interpretation. As noted in that work, the cluster and HII region are not positionally coincident with the peak intensity of the molecular emission, which lies to the West, indicating that the expansion of the HII region finds less resistance in the Eastern

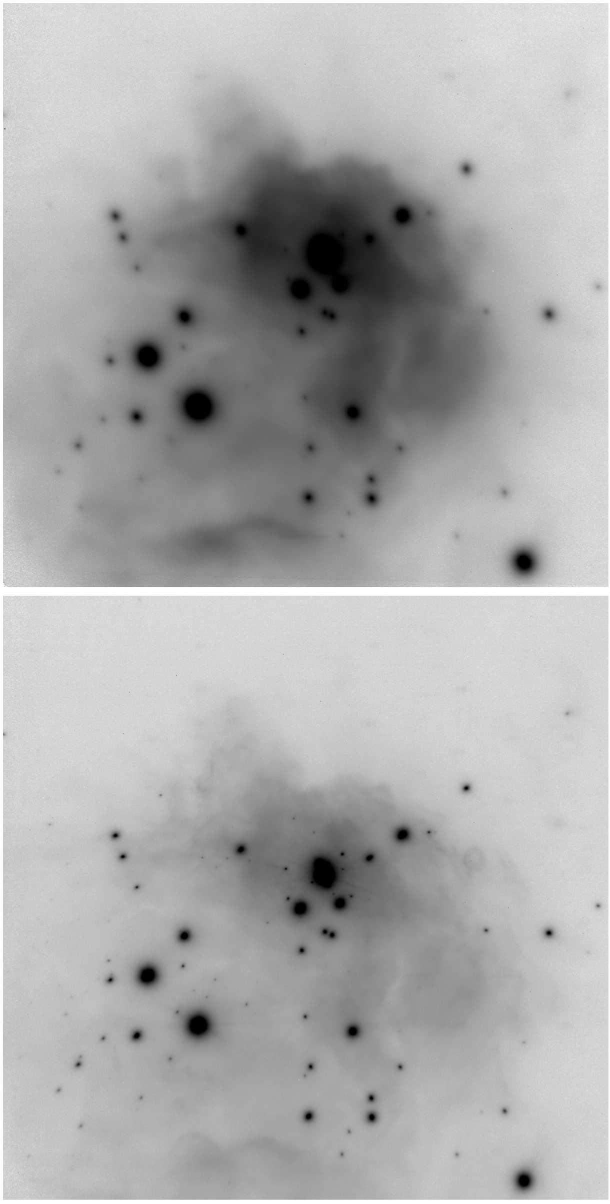

Fig. 2. A comparison between the images obtained through the narrow-band filters centered on the Brγ (*top*) and the H_2 $S(1)\ v = 1 \rightarrow 0$ (*bottom*) lines. Both images are on the same intensity scale. More stars are visible in the H_2 image due to the lower nebular intensity and the better adaptive optics correction. The field covered by each image is $48'' \times 48''$.

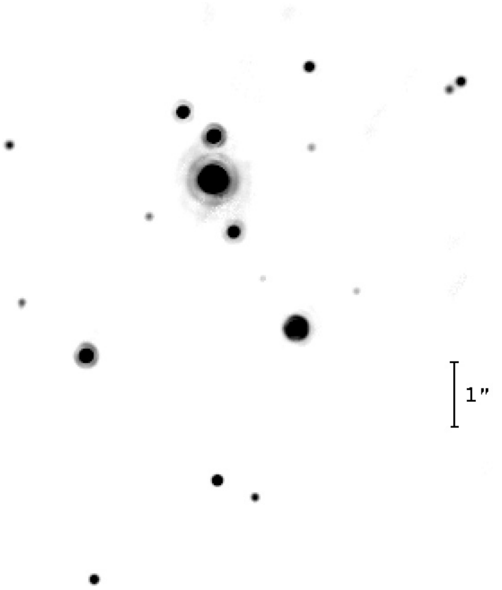

Fig. 3. L'-band image of the region around CSR-012A, the brightest star in the K-band, showing the rich concentration of cluster members around it.

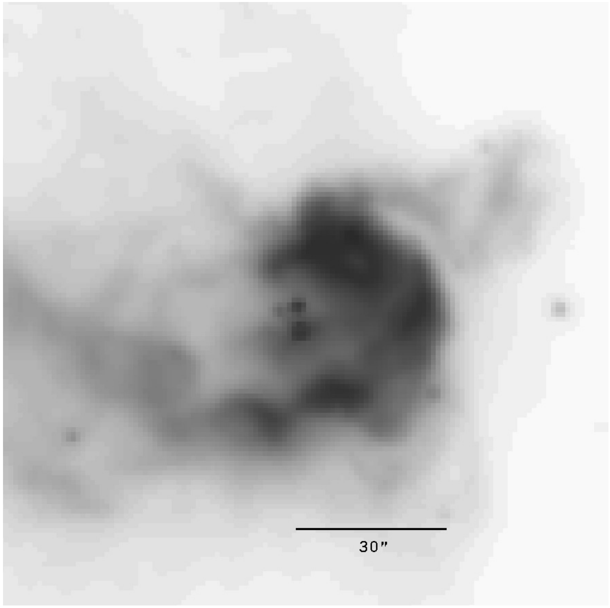

Fig. 4. A wider-field view of the IRAS 16362-4845 region obtained with the IRAC camera on board of the Spitzer space observatory at a central wavelength of 8 μm. The western edge of the nebula is marked by a bright, crescent-shaped rim probably dominated by PAH emission. Some of the brightest cluster members have strong mid-infrared excesses and can be identified in the Spitzer image. The image corresponds to AOR key number 12486912 (Program # 112, "IRAC and IRS observations of RCW 108", Principal Investigator G. Fazio), and has been obtained from the Spitzer archive.

direction. Furthermore, the CO intensity contours presented in CSR05 show a prominent pinching just East from the cluster suggestive of a sharp decrease in column density. Finally, Hα radial velocity maps show a rather sharp change at the same point (see Fig. 8 of CSR05), superimposed on a shallower, larger-scale gradient in the Southwest to Northeast direction seen in both Hα and molecular line observations, as would be expected from an outflow with a component in our direction.

Wider-field images including the surroundings of IRAS 16362-4845 show extended nebular emission towards the East (see Fig. 2 of CSR05), clearly related to the cluster and probably tracing the less dense regions of the ionized outflow, but disconnected from the main body of the compact HII region by a dark patch due to a dense, foreground cloud. The Western border of this cloud appears near the left edge of our NACO images. Interestingly, our H and K_S images show a strip roughly $10'' \times 15''$ across crowded with numerous faint, lightly reddened stars located between the cluster and the dark foreground cloud (see Sect. 3.2). The very confined location of those stars leads us to discard the possibility that they may be cluster members; if they were, most of them would be brown dwarfs based on their faintness and their relatively blue colors. Instead, we consider far more likely that they are background stars seen through a low column density gap just East of the cluster. Although the dust column density in their direction is far lower than that estimated from the molecular gas column density obtained from ^{13}CO $J = 1 \rightarrow 0$ observations of CSR05 (A_V reaching 70 mag near IRAS 16362-4845, as compared to A_V as low as ~10 mag from the colors of those sources), a low extinction hole of the size given above is not ruled out by the ^{13}CO $J = 1 \rightarrow 0$ molecular-line observations at 45″ angular resolution.

3.2. Color–magnitude and color–color diagrams

The color–magnitude diagram of the cluster is presented in Fig. 5. In it we have made a distinction between the sources located in the Western region of high extinction on the background and the Eastern region where, as discussed in the previous section, the extinction appears to be much lower allowing the detection of numerous background sources. For simplicity we have separated the sources in these two categories according to their position with respect to the line $\alpha(2000) = 16^{\rm h}40^{\rm m}01^{\rm s}78$ and we base our discussion on the cluster contents on the Western region alone. The exclusion of the Eastern region, which occupies 20% of our images, is likely to exclude as well some cluster members, but simple visual inspection of Fig. 1 indicates that the vast majority of the cluster members lie in the Western region where contamination by background sources is very low.

The overall appearance of the cluster $(H - K_S)$, K_S diagram presented in Fig. 5 shows a broad distribution in $(H - K_S)$ color which can be due both to variations of the foreground extinction along the line of sight towards each star, and to the varying amounts of infrared excess produced by the circumstellar material associated to each object. Given the deeply embedded nature of the cluster and its youth we expect both causes to significantly contribute. The existence of sources with large amounts of circumstellar dust reprocessing the light of the central object is confirmed by the $(J-H)$, $(H-K_S)$ diagram (Fig. 6) and, most clearly, by the $(H-K_S)$, (K_S-L') diagram (Fig. 7), where many stars (in the latter diagram, most of them) lie to the right of the reddening vector delimiting the region of the diagrams accessible to normal photospheres obscured by different amounts of extinction; see Sect. 3.4. For reference, the solid line in those diagrams is the unreddened 1 Myr isochrone using the evolutionary models of Palla & Stahler (1999), complemented with the JHK_S colors computed for them by Testi et al. (1999) and shifted to our adopted distance modulus $DM = 10.6$.

The isochrone plotted in Fig. 5 demonstrates the sensitivity of our observations to the entire range of stellar masses and even to massive brown dwarfs. The upper end of the isochrone shown in this figure corresponds to a mass of 30 $M_{\odot}$, whereas the lowest end marks the position of a 0.01 $M_{\odot}$ brown dwarf.

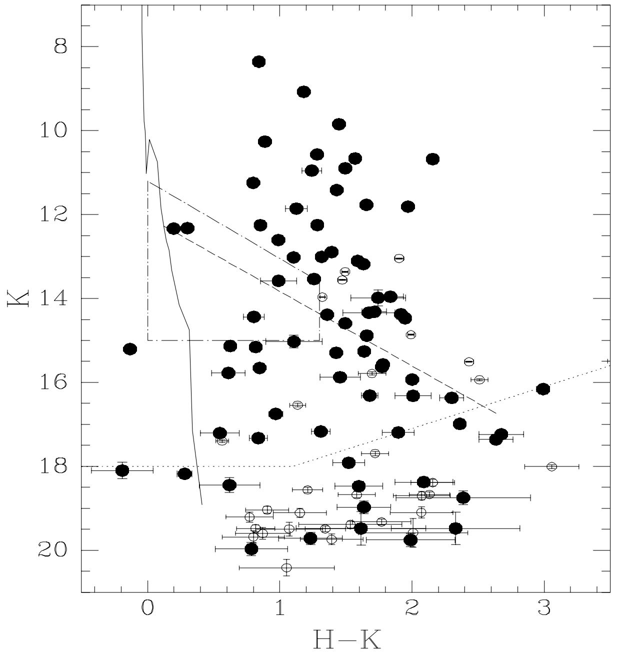

Fig. 5. $(H - K_S), K_S$ color–magnitude diagram of the IRAS 16362-4845 cluster. Full large dots are stars located in the region dominated by the cluster, whereas the small open circles are objects located in the low-extinction region to the East of $\alpha(2000) = 16^h40^m01^s.7$ and dominated by faint background sources. The dotted line marks the position of the completeness limits in H and K_S given in Table 3. The solid line is the 1 Myr isochrone of the models of Palla & Stahler (1999) using the infrared colors derived by Testi et al. (1999). The dashed line marks the position of a 1 $M_\odot$ star obscured by varying amounts of extinction. The lower right end of the line corresponds to $A_V = 40$ mag. Finally, the dot-dashed line delimits the area where CSR05 noted an absence of faint, lightly reddened stars, which is further discussed in Sect. 3.2. The bottom of the area corresponds to the approximate detection limit of the observations of CSR05.

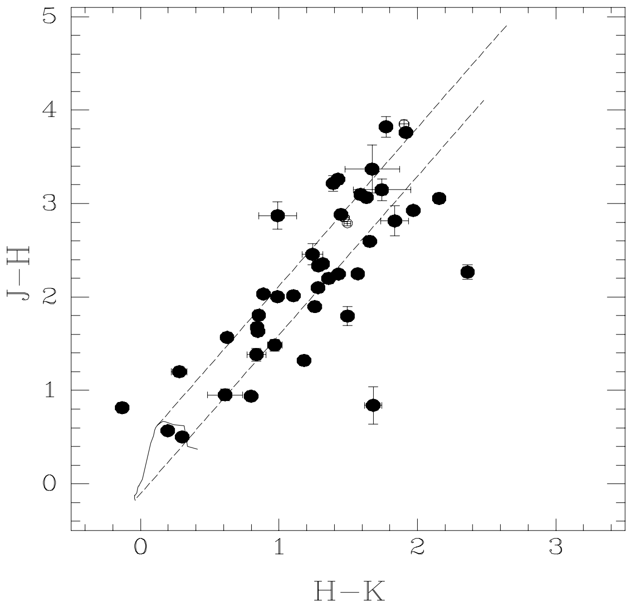

Fig. 6. $(H - K_S)$, $(J - H)$ color–color diagram of the IRAS 16362-4845 cluster. Symbols are the same as in Fig. 5. The solid line represents the position of 1 Myr old unreddened stars with no circumstellar infrared excess from the models of Palla & Stahler (1999). The dashed lines are reddening vector whose lengths corresponds to an extinction $A_V = 40$ mag. The top vector has its origin at the position of a 1 $M_\odot$ star, and the bottom has its origin at the position of an early O-type star. This latter vector delimits the area accessible to a normal photosphere reddened by extinction, and the position of objects to the right of this line denotes the existence of infrared excess.

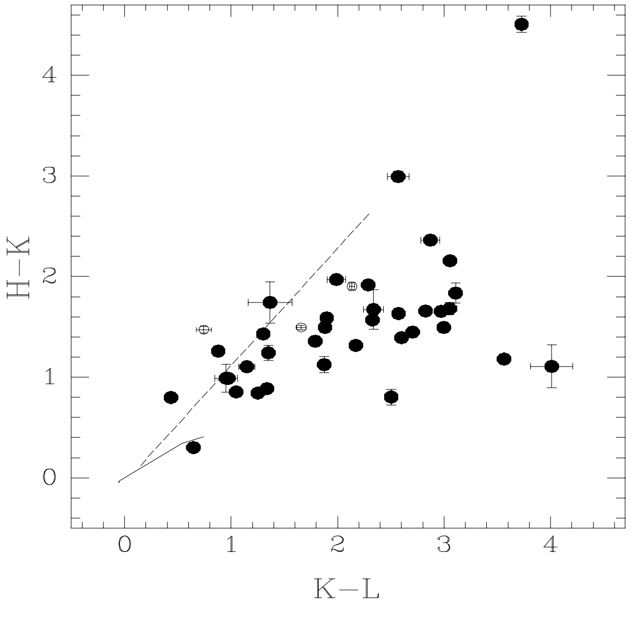

Fig. 7. $(K_S - L')$, $(H - K_S)$ color–color diagram of the IRAS 16362-4845 cluster. Symbols and lines have the same meaning as in Fig. 6, but now we have not plotted the reddening vector with its origin at the position of a O-type star (bottom left end of the solid line) since it does not separate anymore the regions accessible and inaccessible to normal photospheres reddened by extinction.

Because of the narrow range of infrared colors covered by normal stars, the main effect of assuming a different cluster age is to shift the isochrone vertically in the color–magnitude diagram, thus changing the mass corresponding to an object of a given absolute magnitude in the sense of the mass being lower for a younger assumed age. Although the precise masses of the intrinsically faintest objects detected in our images critically depend on the age of the cluster, we can confidently state that the completeness limit of our observations probes the brown dwarf regime for any plausible age of the cluster. Indeed, a star at the hydrogen-burning limit ($M = 0.078$ $M_\odot$) reaches an absolute magnitude $M_K = 6.5$ (corresponding to our completeness limit $K = 18.1$ minus the adopted $DM = 10.6$ of the cluster, obscured by a foreground extinction of $A_K = 1$ mag) at an age of 6 Myr (Baraffe et al. 2003). The age of the IRAS 16362-4845 cluster is likely to be much less than that (see Sects. 9 and 4).

It is interesting to compare the results obtained here with the claim made in CSR05 about the apparent lack of cluster members in the $(H - K_S)$, K_S diagram lying below an extinction vector having its origin near the position of a main-sequence A0 star. Given the severe incompleteness of the observations presented in CSR05 above $K_S \simeq 15$ in the area of the cluster due to the bright nebulosity, the region of the color–magnitude diagram that was claimed to be devoid of stars in that work is effectively delimited by the polygon joining the points $[(H - K_S), K_S] = (0, 11.2), (0, 15.0), (1.3, 15.0)$, and $(1.3, 13.6)$, where only the likely foreground star CSR-013 is detected in their observations. Our present work reveals four stars in that area, whose non-detection in CSR05 is readily explained by examining their location: one of them, CSR-012E, is a faint companion just 1″1 from the bright star CSR-012A. The second is CSR-008B, very close (0″22) to the blue, likely foreground star CSR-008A. The third is CSR-008A itself, to which CSR05 allocated an infrared excess that our new observations show to be actually due to the presence of the much redder component B. The true $(H - K_S)$ color is consistent with it being a foreground, lightly reddened star when component B is excluded. Finally, the fourth star CS-104, is faint and near CSR-012A, only 1″5. The depopulation of that area of the color–magnitude diagram in CSR05 is thus real, as only close companions to other stars populate it in the present study.

3.3. Correcting for extinction and infrared excess

Near-infrared observations, most notably in the K_S band, present well known advantages for the observational characterization of the population of a cluster: they allow one to probe down to very low masses given that most of the luminous output of the least massive stars and brown dwarfs lies in the near-infrared, and they reduce the effects of extinction with respect to shorter wavelength bands. Nevertheless, the K_S band also probes a spectral region where circumstellar emission can significantly contribute to the luminosity of star and even dominate over the photosphere, and the greater transparency of dust at that wavelength increases the level of contamination of background sources for clusters residing in clouds of low or moderate column density. Although the large dynamic range in luminosity covered by our observations is in principle a very useful resource to study the stellar population of IRAS16362-4845 over a wide range of masses, the particular conditions of the cluster require special care in both deriving and interpreting the properties of its members.

To approximately correct the observed magnitudes for the effects of extinction and circumstellar emission, let us write the observed magnitude of a star in each of the J, H, and K_S bands[3] as

$$m_\lambda = m_{\lambda 0} + A_\lambda + E_\lambda \tag{1}$$

where m_λ is the magnitude in one of those bands, $m_{\lambda 0}$ is the magnitude free of extinction and infrared excess given by the model isochrone used, A_λ is the extinction, and E_λ is the infrared excess. The values of A_λ are related by the extinction law; adopting the standard values from Rieke & Lebofsky (1985), $A_J = 2.518 A_{K_S}$, $A_H = 1.563 A_{K_S}$. On the other hand, circumstellar disk models show that the values of E_λ are in general related. Extensive grids of models such as those computed by Lada & Adams (1992) for Herbig Ae/Be stars and classical T Tauri star disks indicate that families of models produce shifts in the $(J - H)$, $(H - K_S)$ diagram that can be approximately characterized by an *infrared excess vector* with a slope $\beta = \Delta(J - H)/\Delta(H - K_S)$. A good approximation for classical T Tauri stars with surface temperatures $T = 3000$ K is $\beta \simeq 0.75$, similar to the values derived from the disk models of Meyer et al. (1997). For Herbig Ae/Be stars with disks having central holes and inner edge temperatures $T = 2000$ K, which generally provide the best fits to the observed colors of these objects, $\beta \simeq 0.56$. If we assume a negligible infrared excess at J, where the ratio between luminosity reprocessed at the disk and photospheric flux is lowest, the approximate condition $E_J = 0$ leads to

$$E_H = \beta/(\beta + 1) E_{K_S} \tag{2}$$

implying $E_H = 0.43 E_{K_S}$ for Herbig Ae/Be stars and $E_H = 0.36 E_{K_S}$ for classical T Tauri stars. We thus adopt $E_H = 0.39 E_{K_S}$ for our analysis as an average value characterizing the typical value of the circumstellar excess vector. Finally, since the model isochrones provide values of (J_0, H_0, K_{S0}) at n discrete masses rather than a continuous curve, we must interpolate between the given points. We do this by means of a simple linear interpolation, such that the line joining two points i and $i + 1$ of the isochrone is approximated by a straight segment parametrized by the continuous variable ξ. Taking all this into account, Eq. (1) becomes

$$J = J_{0i} + \xi(J_{0i+1} - J_{0i}) + 2.518 A_K \tag{3a}$$

$$H = H_{0i} + \xi(H_{0i+1} - H_{0i}) + 1.563 A_K - 0.39 E_K \tag{3b}$$

$$K_S = K_{S0i} + \xi(K_{S0i+1} - K_{S0i}) + A_K - E_K \tag{3c}$$

where J_{0i}, H_{0i}, K_{S0i} are the magnitudes given by the models at the isochrone point i. The solution to system (3) yields the values of the three unknowns ξ, A_K, and E_K. It may be noticed that a similar procedure has been recently used by Figuerêdo et al. (2005) in their analysis of the cluster associated to the giant HII region G333.1-0.4. They correct for infrared excess assuming that it is noticeable only in K_S, and then correct of extinction by dereddening along the limiting reddening vector in the $(J - H)$, $(H - K_S)$ diagram marking the boundary of the region accessible by objects free of infrared excess. As those authors point out, this procedure yields a lower limit to E_K, as well as an overestimate of A_K, and is equivalent to setting $\beta = 0$ in Eq. (2). However, both models and observations suggest that the excess at H cannot be neglected in general. Furthermore, the method that we have used does not use the limiting reddening vector, but an actual reddening vector having its origin at the photospheric colors of the best fitting theoretical model instead.

For the stars having measured magnitudes in the J, H, and K_S filters we have solved the system (3) for $1 \le i \le n - 1$, taking as the best solution the one for which $0 \le \xi \le 1$, i.e., for which the best fitting model is an interpolation between consecutive points along the isochrone. As may be noticed in Fig. 5, isochrones within a certain range of young ages present a kink giving rise to a small mass interval in which stars of a given mass are brighter than those slightly more massive, due to their slower evolutionary rate. In those narrow intervals it is possible to find more than one solution to the system (2) with $0 \le \xi \le 1$. This is of little practical concern, as the values of A_K and E_K, and of J_0, H_0, K_{S0} are very similar for all solutions. The derivation of the K luminosity function (see Sect. 3.5) is thus hardly affected by the choice of the solution in those kinks.

The fitting procedure described above yields unphysical solutions for some objects, with slightly negative values of either A_K or E_K that may be due to photometric errors, to the simplifications adopted for the reddening and infrared excess corrections, or to deviations between the colors predicted by the models and those of the actual stars. We have dealt with the cases where the solution to Eqs. (3) yields $E_K < 0$ by solving the system again by least squares, setting E_K to zero. On the other hand, the only case in which the solution to Eqs. (3) yields $A_K < 0$ corresponds to the object farthest to the right of the limiting reddening vector in the $(J - H)$, $(H - K_S)$ diagram. For this star

---

[3] L' measurements are also available for many stars near the center of the cluster, and the procedure described here can in principle be easily extended towards that band as well. Nevertheless, since L' strongly dominates over the photosphere for many objects in our sample, the fit would become greatly sensitive to the approximation used to represent the excess in that band, which is necessarily rough. We have thus preferred to base our analysis on the JHK_S bands alone.

Table 4. Objects with infrared excess.

Star	α(2000)	δ(2000)	K_S	$J-H$	$H-K_S$	K_S-L'	M_K	A_V	E_K
CSR-002	16:39:58.6	–48:52:05	10.568 ± 0.010	2.098 ± 0.014	1.282 ± 0.014	–	−2.3	20.6	0.04
CS-096	16:40:00.3	–48:51:56	15.777 ± 0.114	0.952 ± 0.063	0.611 ± 0.127	–	5.0	3.0	0.16
CSR-014	16:40:00.3	–48:51:55	13.537 ± 0.008	1.896 ± 0.030	1.259 ± 0.022	0.879 ± 0.052	2.9	8.2	0.91
CSR-009A	16:39:59.9	–48:51:53	11.242 ± 0.006	0.938 ± 0.007	0.798 ± 0.008	0.435 ± 0.018	0.5	6.6	0.64
CSR-018	16:40:01.2	–48:51:52	9.074 ± 0.010	1.320 ± 0.014	1.181 ± 0.014	3.564 ± 0.021	−1.6	9.8	0.98
CS-097	16:40:00.3	–48:51:51	14.388 ± 0.018	2.198 ± 0.056	1.358 ± 0.035	1.790 ± 0.059	3.1	12.0	0.66
CSR-015	16:40:00.3	–48:51:46	13.008 ± 0.008	2.355 ± 0.042	1.316 ± 0.034	2.171 ± 0.023	0.9	16.1	0.35
CSR-019A	16:40:01.3	–48:51:45	11.415 ± 0.008	2.245 ± 0.007	1.430 ± 0.010	1.302 ± 0.026	−1.4	21.3	0.20
CSR-001	16:39:58.3	–48:51:45	13.020 ± 0.005	2.013 ± 0.028	1.104 ± 0.027	1.148 ± 0.075	1.5	11.9	0.41
CSR-010A	16:40:00.0	–48:51:42	10.662 ± 0.006	2.247 ± 0.021	1.569 ± 0.012	2.328 ± 0.022	−1.6	20.0	0.56
CSR-010B	16:39:59.9	–48:51:42	13.985 ± 0.191	3.146 ± 0.117	1.743 ± 0.207	1.366 ± 0.206	0.9	23.9	0.25
CSR-010C	16:40:00.0	–48:51:42	16.315 ± 0.040	0.840 ± 0.199	1.681 ± 0.063	3.052 ± 0.069	6.4	3.8	1.11[1]
CSR-012B	16:40:00.1	–48:51:40	10.897 ± 0.025	1.795 ± 0.099	1.495 ± 0.047	1.882 ± 0.034	0.0	12.8	1.15
CSR-023	16:40:01.7	–48:51:38	13.362 ± 0.011	2.786 ± 0.025	1.494 ± 0.024	1.658 ± 0.045	0.2	22.7	0.01
CS-103	16:40:00.0	–48:51:38	13.959 ± 0.041	2.814 ± 0.161	1.836 ± 0.100	3.109 ± 0.044	2.6	16.3	1.05
CSR-017	16:40:00.8	–48:51:38	11.769 ± 0.009	2.595 ± 0.042	1.655 ± 0.030	2.972 ± 0.026	−1.3	24.4	0.25
CSR-005B	16:39:59.5	–48:51:37	11.811 ± 0.016	2.926 ± 0.016	1.970 ± 0.019	1.989 ± 0.086	−1.2	26.3	0.56
CSR-005A	16:39:59.5	–48:51:37	10.679 ± 0.008	3.055 ± 0.011	2.157 ± 0.009	3.056 ± 0.020	−3.0	30.8	0.40
CS-099	16:40:00.2	–48:51:37	16.990 ± 0.019	2.266 ± 0.078	2.362 ± 0.033	2.872 ± 0.089	7.7	9.2	2.31
CS-064	16:40:01.4	–48:51:33	16.752 ± 0.027	1.485 ± 0.062	0.969 ± 0.052	–	5.4	8.3	0.20

[1] Fit obtained with $\beta = 0$ in Eqs. (3) (i.e., no H-band excess), as $A_V < 0$ would be obtained otherwise.

we have assumed that all the excess lies in the K_S band and we have solved Eqs. (3) again, now replacing the coefficient 0.39 in Eq. (3b) that accounts for the H-band excess by zero, thus obtaining solutions in which both A_K and E_K are positive. This might be an object possessing a large central hole devoid of the hot dust component that provides the main contribution to the infrared excess at the shorter wavelengths.

Finally, many of the fainter objects in our sample have measurements in only two bands, generally H and K_S. We have assumed that they do not have infrared excess and have solved the relevant subset of Eqs. (3) for ξ and A_K. Since our results for the objects with measurements in J, H, and K_S show that somewhat more than half do not require infrared excess, and that for those that do the appropriate value of E_K is generally small (see Sect. 3.4) we do not expect that the assumption of E_K for objects with only one measured color introduces a significant bias.

3.4. Infrared excesses

The list of stars for which an infrared excess in the K band is needed to obtain a good fit to the colors predicted by the models using Eqs. (3) is given in Table 4. Taking into account that the total number of sources having JHK_S measurements in our sample is 44, our results imply that infrared excesses need to be assumed for 45% of the stars in order to fit their JHK_S colors. This fraction is uncertain and the derived infrared excess may be spurious in some cases, as the values of E_K often are of the order of the combined uncertainties arising from the photometry and the modeling of the circumstellar emission. Indeed, even in the cases where the fit suggests the presence of infrared excess we find $E_K < 0.75$ (implying that most of the emission arises from the photosphere rather than from reprocessing by the circumstellar environment) for 15 out of 21 stars, and only 4 objects require $E_K > 1.0$. It must be noted that the limitation of this analysis to stars detected at J, H, and K_S leads us to consider objects that have cleared most of their circumstellar envelopes and are thus detectable at those wavelengths. Observations at longer wavelengths reveal few additional objects that have not reached that stage, and are discussed in Sect. 3.7.

3.5. The K luminosity function

The luminosity function in the K band is frequently used in studies of young clusters as a diagnostic tool of the mass function and the star formation history of their stellar populations. Pioneering work on the interpretation of the K luminosity function was presented by Zinnecker et al. (1993). More recently, Muench et al. (2000) have carried out extensive modeling of the K luminosity function (hereafter KLF) showing its dependence on factors such as the cluster age, the spread of star formation over time, and the choice of theoretical pre-main sequence evolutionary tracks.

To derive the KLF[4] of IRAS 16362-4845 we have derived intrinsic K_S magnitudes using the method described in the previous Section for all the stars detected in at least two of the JHK_S bands. We have excluded a few sources with $H - K_S < 0.5$, as they are most likely foreground stars. Also, we have considered components of close binary systems as separate stars only when reliable photometry could be obtained for each of them (see Sect. 3.6). Since we are excluding the Easternmost area of the imaged field due to the apparent extinction hole in that region, as described in Sect. 3.2, we expect the population analyzed here to be strongly dominated by cluster members, as the thick dust column provides an efficient screen against the background population even at the K_S band. A few sources have very red colors and may be background to the cluster, but as discussed in Sect. 3.7 this is unlikely to be the case even for the reddest sources.

The KLF that we derive is potentially affected by several biases that must be carefully taken into account. In addition to the varying detection thresholds across the field discussed in Sect. 2.3, the varying level of foreground extinction implies that

---

[4] More rigorously we should instead refer to the K_S luminosity function here. However, the difference between the magnitude of any of the stars in our sample in the K and K_S bands is virtually irrelevant for our purposes, as it is much smaller than the size of the bins used to build the KLF and the size of the errors introduced by our rather schematic corrections for extinction and infrared excess. We thus use the name K luminosity function as is normally done in the literature.

the sampled volume of the cluster becomes progressive smaller for intrinsically fainter sources, as the most obscured objects of a given intrinsic luminosity fall below the detection limit. On the other hand, some faint members that would have remained undetected if their emission were purely photospheric may be brought above the detection threshold by their infrared excess. However, based on the moderate or altogether absent K_S-band excesses that we generally obtain for the stars having JHK_S photometry, we estimate the influence of infrared excesses to be small in the derivation of the KLF.

To minimize the bias due to the variable sampling of the cluster volume due to extinction, we have obtained a KLF by considering only stars having $A_V < 23.8$ and $M_K < 4.0$. Both constraints are related by the condition that the intrinsically faintest and most obscured stars in such sample are at the overall completeness limit of our observations (see Table 3). Indeed, a star with $M_K = 4.0$ obscured by $A_V = 23.8$ mag would have $H = 19.1$, $K_S = 17.3$ and would thus be detected anywhere in the cluster, as would be any star with a brighter absolute magnitude and reddened by a smaller amount. Our choice of the limiting absolute magnitude and extinction is a compromise between the need to include a statistically representative sample of the cluster population (which requires a limiting extinction as high as possible) and to probe the KLF down to low enough masses. Concerning the latter, $M_K = 4.0$ corresponds to a mass $M \simeq 0.15\ M_\odot$ at an age of 1 Myr, the precise mass being only approximate due to the large uncertainties in low-mass evolutionary tracks at such early ages (Baraffe et al. 2002). Our magnitude-limited KLF, presented in Fig. 8, thus covers nearly the whole range of stellar masses.

The most intriguing feature of the KLF of the IRAS 16362-4845 cluster is its flatness over virtually the entire absolute magnitude range covered by our observations, which supports the hints of a *top heavy* luminosity function reported in CSR05. Similar indications are found in the KLF independently derived by Wolk et al. (2007) for the X-ray selected population of RCW 108, where the central region containing IRAS 16362-4845 has a KLF remarkably flatter than that of the surrounding area. This is in contrast with the results of most other studies of embedded clusters in the literature, which obtain KLFs rising towards fainter absolute magnitudes, with a particularly sharp increase in number counts in the $0 < M_K < 2$ interval. For reference, we show in Fig. 8 the shape of the KLF of the Trapezium cluster (Muench et al 2002). Similar results are obtained on the clusters embedded in galactic giant HII regions (Figuerêdo et al. 2005, and references therein), as well as for other embedded clusters containing massive stars (e.g. Leistra et al. 2006; Massi et al. 2006; Fujiyoshi et al. 2005; Muench et al. 2003, for recent work). Although very low mass stars and even brown dwarfs appear to be present in the cluster coexisting with its most massive members, they do so in numbers far smaller than expected from a normal IMF (e.g. Kroupa 2001).

It is hard to explain the flat shape of the extinction-limited KLF as a result of incompleteness or incorrect assumptions solely. The steepness of the KLFs of other clusters is well detected at $M_K < 2$, which is two full magnitudes brighter than the limit of our extinction- and magnitude-limited sample. The flatness of our KLF that we obtain thus cannot be attributed to the possible inaccuracy of the limiting magnitudes listed in Table 3.

On the other hand, an underestimated infrared excesses would lead to a derived absolute magnitude that is brighter than the actual one, as both the extinction and the photospheric flux are then overestimated. Therefore, the possibility exists in principle that objects populating the brighter bins of Fig. 8 may actually be intrinsically fainter objects with strong infrared excess that has not been properly taken into account. The required size of the discrepancy between the actual and the derived infrared excesses should be significantly larger than the bin size of our KLF in order to have a noticeable impact on its shape. However, such large infrared excesses would imply negative extinctions for many of the objects of the cluster, and we can thus rule out this as a significant contributing effect. A systematic underestimate of the infrared excess may also have taken place among the objects undetected at J, as we have assumed $E_K = 0$ for them. However, those tend to be faint objects at H and K_S contributing to the faintest magnitude bins of the KLF, which may thus contain objects that would have been excluded had the infrared excess been properly taken into account. Since the lack of J measurements is more common towards fainter magnitudes, the systematically neglected infrared excesses among such objects should lead to our KLF being *steeper* than the actual one, and thus cannot account for the derived flatness. Finally, a systematic underestimate of the luminosity among the brightest objects may also result if the value of β that we have adopted in Eqs. (2) were smaller than the actual one, leading to the underestimate of the excess at H and the invalidity of our assumption $E_J \simeq 0$. We note nevertheless that a larger value of β would imply that the dust responsible for the infrared excess should be significantly hotter than the dust sublimation temperature in order to produce colors similar to those of the underlying objects, which we consider highly implausible. We are thus inclined to consider the remarkably flat shape of the KLF of

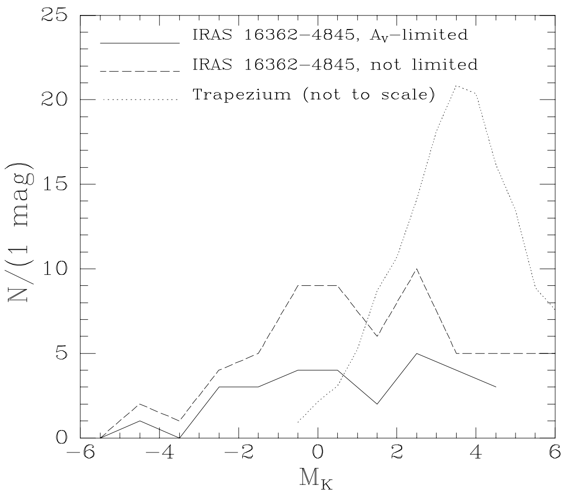

Fig. 8. The K luminosity function (KLF) of the IRAS16362-4845 embedded cluster, expressed as number of stars per 1 mag bin. The solid line corresponds to the extinction-limited sample that considers members with line-of-sight extinctions $A_V < 23.8$, which is complete down to $M_K = 4.0$. An unrestricted KLF including all the cluster members (as well as possibly a few very reddened background stars) is represented by the dashed line. This latter KLF is virtually complete for the brightest bins, but becomes progressively incomplete as fainter stars become undetectable due to extinction. Finally, the KLF derived by Muench et al. (2002) for the Trapezium cluster is shown for reference, scaled by an arbitrary factor for convenience in the representation. The absolute magnitude scale for the Trapezium has been set by assuming its distance modulus to be 8.0, as used by those authors. No correction for extinction has been applied to the Trapezium KLF. Given that the vast majority of the Trapezium members have extinctions below $A_K = 0.5$ (see Fig. 4a of Muench et al. 2002), a mean extinction correction would shift the Trapezium KLF by less than one bin towards the left.

IRAS 16362-4845 as a real feature of the cluster, and we discuss its implications in Sect. 4.

The mass of the IRAS 16362-4845 cluster was crudely estimated by CSR05 to be about 210 $M_{\odot}$. The new observations allow us to refine that estimate by providing a deeper and more accurate census of its members, based on the more detailed estimate of individual stellar parameters described in Sect. 3.3. The cluster mass derived from stars detected in at least two of the $JHK_{\rm S}$ bands amounts to 370 $M_{\odot}$. The difference is due to the fact that CSR05 based their estimate on the number of stars above the absolute magnitude of a main sequence A0V star and assuming that the cluster population follows a log-normal Miller & Scalo (1979) IMF, rather than on the individual masses. Applying the same method to the new observations presented here taking into account the stars more massive than 1 $M_{\odot}$ (the dashed line in Fig. 5) we obtain a cluster mass of only 120 $M_{\odot}$. The lower masses obtained with this method are easily explained by the fact that the mass function underlying the KLF is flatter than the log-normal Miller & Scalo (1979) IMF, and that the average mass of the stars above a certain threshold is therefore greater than the average mass expected from the assumed IMF. We note by passing that our new determination, 370 $M_{\odot}$, changes little due to the incompleteness of the census at very low masses, since their contribution to the cluster total mass is very small given the flatness of the IMF. It is also fairly insensitive to the assumed age, as the massive stars dominating the mass of the cluster evolve very rapidly towards the main sequence.

3.6. Bright, close multiple systems

It is a well known observational fact that binaries with mass ratios close to unity are very common among massive stars (e.g. Garmany et al. 1982; Mason et al. 1998; Preibisch et al. 1999; García & Mermilliod 2001). Close binarity among massive stars actually places important constraints on their proposed formation mechanisms (e.g. Bonnell et al. 1998; Yorke & Sonnthaler 2002; Bonnell 2005; Beuther et al. 2007) and has been usually linked to the fact that virtually all massive stars are formed in dense cluster environments, where dynamical interactions among cluster members and with the accreting gas can dominate their early evolution. Such interactions favor the formation of bound systems, while subsequent accretion causes high mass ratios and orbital evolution towards shorter separations between their members (Bate et al. 2003; it may be noted however that a high fraction of wide binaries with low mass ratios has been observed in the young but dynamically evolved cluster NGC 6611 by Duchêne et al. 2001). Observations of dense clusters containing very young massive stars, or even massive stars still deeply embedded in their parental material, suggests that close binarity arises very early in their evolution (Bosch et al. 2001; Apai et al. 2007).

The diffraction-limited quality of our observations in the L' band allows us to search for visual pairs among the bright members of the IRAS 16362-4845 cluster with angular separations below $0''1$, corresponding to a projected distance of 130 AU, and $JHK_{\rm S}$ photometry of the individual components can be obtained for pairs separated by more than $\simeq 0''2-0''3$. We constrain ourselves to the central area of the cluster covered by the L' images (Sect. 2.1), as the image quality in that band (and therefore the shortest separations that can be measured) is nearly uniform across the entire field. We also consider exclusively the brighter pairs in which both components are detected at L', since crowding at fainter magnitudes in the H or $K_{\rm S}$ bands makes it impossible to separate true wide binaries from chance alignments or unrelated sources. We have set the upper limit of the separation for stars to be considered as close pairs to $1''1$ (1430 AU projected distance), as this is the distance of the farthest star of the distinct subcluster of five members around CSR 012A, where the stellar density in our images peaks (see Fig. 3). Unfortunately our results are of limited value in order to determine the physical characteristics of the detected systems, given the frequent existence of excess emission in the L' band (Sect. 3.2) and the lack of a precise age determination of the cluster, which prevent us from deriving masses and mass ratios. However, our findings should include all the massive stars in the cluster with separations in the $0''1-1''1$ range, and can thus form a basis for future statistical studies of its massive binary star content.

The multiple systems that we detect are listed in Table 5. These systems include the CSR 012 cluster of five members, the rather loose possibly triple system CSR 010, and the likely casual arrangement of unrelated objects CSR 008. The bluest component of the latter, CSR 008A, is the brightest star in the nebula at visible wavelengths and the very light reddening indicated by its visible and infrared colors suggests that it is a foreground star. However, it was noted in CSR05 that its infrared photometry shows a clear $K_{\rm S}$-band excess hinting at true cluster membership. The superior resolution of the observations presented here offer the solution to the puzzle, showing that CSR 008A has a redder companion at only $0''22$. Although such close chance alignment is highly unlikely, we believe that the widely different infrared colors of both components convincingly argues for true membership in IRAS 16362-4845 of component B only, leaving component A as an ordinary foreground star. Finally, we include in our list star CS-093, which appears elongated in the $K_{\rm S}$-band images and shows a faint, short tail to the South in the L'-band images. We consider this to be most likely due to a fainter, marginally resolved companion at $\sim 0''06$ (80 AU projected distance) from the primary star.

Excluding the likely foreground source CSR 008A and considering CS-093 as two separate stars, the results listed in Table 5 indicate that 18 of the 42 sources detected in the L' band reside in 7 multiple systems with projected separations from the primary between 80 and 1430 AU, out of which 5 are binary systems, corresponding to a multiplicity fraction of 0.43[5]. As noted above, our criterion of detection of both components in the L' band is rather loose in terms of the lowest masses represented in Table 5, as some components may be detected thanks to their infrared excess rather than to the intrinsic brightness (and mass) of the central star. Assuming that the frequency and amount of L' excesses are the same among components of multiple systems and single stars, the multiplicity fraction that we have derived above should nevertheless remain unaffected by this caveat. In principle such assumption may not be taken for granted, as multiplicity can affect the timescale for dissipation of the inner disks responsible for the L' excess. However, we find no evidence for any

---

[5] We define the multiplicity fraction as

$$\frac{\sum_{n=2}^{\infty} nS_n}{\sum_{n=1}^{\infty} nS_n},$$

where S_n is the number of systems containing n stars; this is, the number of stars in multiple systems divided by the total number of stars. An alternative definition used by other authors (e.g. Duchêne et al. 2001) is $\sum_{n=2}^{\infty} S_n / \sum_{n=1}^{\infty} S_n$, i.e., the number of multiple systems over the total number of systems, including single stars. Using this second definition we obtain a multiplicity fraction of 0.21, which is close to the value 0.18 found by Duchêne for NGC 6611 also using adaptive optics observations.

Table 5. Close pairs in the L' band.

Star	α(2000)[1]	δ(2000)[1]	J	H	K_S	L'	Separation	Position angle
CSR-009A	16:39:59.9	–48:51:53	12.978 ± 0.004	12.040 ± 0.006	11.242 ± 0.006	10.807 ± 0.017		
CSR-009B			–	–	–	11.147 ± 0.044	0″13	85°6
CSR-019A	16:40:01.3	–48:51:45	15.090 ± 0.004	12.845 ± 0.006	11.415 ± 0.008	10.113 ± 0.025		
CSR-019B			–	–	–	10.969 ± 0.045	0″18	220°2
CSR-011A	16:40:00.1	–48:51:45	17.502 ± 0.075	14.286 ± 0.034	12.894 ± 0.016	10.293 ± 0.015		
CSR-011B			15.598 ± 0.014	13.596 ± 0.029	12.607 ± 0.013	11.633 ± 0.030	0″62	245°5
CSR-010A	16:40:00.0	–48:51:42	14.478 ± 0.018	12.231 ± 0.010	10.662 ± 0.006	8.334 ± 0.021		
CSR-010B			18.874 ± 0.084	15.728 ± 0.081	13.985 ± 0.191	12.619 ± 0.076	1″07	300°9
CSR-010C			18.836 ± 0.193	17.996 ± 0.049	16.315 ± 0.040	13.263 ± 0.056	0″89	34°0
CS-093	16:40:00.4	–48:51:42	19.382 ± 0.187	16.014 ± 0.176	14.341 ± 0.088	12.003 ± 0.030	[2]	
CSR-012A	16:40:00.1	–48:51:40	10.872 ± 0.010	9.198 ± 0.010	8.356 ± 0.010	7.105 ± 0.025		
CSR-012B			14.187 ± 0.091	12.392 ± 0.040	10.897 ± 0.025	9.015 ± 0.023	0″65	358°2
CSR-012D			–	12.981 ± 0.064	11.856 ± 0.050	9.981 ± 0.014	0″87	202°4
CSR-012E			17.441 ± 0.113	14.571 ± 0.094	13.581 ± 0.099	12.628 ± 0.046	1″10	119°4
CSR-012C			14.651 ± 0.099	12.195 ± 0.053	10.953 ± 0.050	9.603 ± 0.020	1″09	23°3
CSR-008A	16:39:59.7	–48:51:39	13.127 ± 0.017	12.625 ± 0.022	12.324 ± 0.012	11.677 ± 0.039		
CSR-008B[3]			–	16.135 ± 0.150	15.028 ± 0.150	11.017 ± 0.025	0″22	307°4
CSR-005A	16:39:59.5	–48:51:37	16.146 ± 0.010	12.823 ± 0.005	10.679 ± 0.008	7.878 ± 0.018		
CSR-005B			16.707 ± 0.011	13.781 ± 0.011	11.811 ± 0.016	9.822 ± 0.085	0″27	138°0

[1] Coordinates of the primary component. [2] Extension approximately 0″06 long towards position angle 170°, probably caused by a faint, marginally resolved companion. [3] Probably not a true binary but a chance alignment: CSR-008A is a likely unrelated foreground star, and CSR-008B a cluster member.

systematic differences between members of multiple systems and single stars when considering their positions in the ($H - K_S$), ($K_S - L'$) diagram (Fig. 7).

As illustrated by the discussion of the observations of NGC 6611 by Duchêne et al. (2001), completeness corrections in binarity studies require that one carefully takes into consideration instrumental effects, contamination by unrelated sources, extrapolations beyond the range of separations probed by the observations, and assumptions on the statistics of orbital parameters. Comparisons among different studies are furthermore hampered by the different observing techniques, instruments, and wavelength regions used. Leaving aside the difficulties of an unbiased comparison, we can say that our results indicate a high multiplicity fraction among the brightest members, and the lower limit that we find (at least 43% of the massive stars in the cluster residing in binaries) suggests that, like in other clusters, most of the massive stars in IRAS 16362-4845 may be part of multiple systems.

3.7. Very red objects

The bulk of the stars projected on the area of the nebula and its surroundings have near infrared colors indicating extinctions in the $10 < A_V < 30$ magnitude range. However, a few objects listed in Table 6 display $H - K_S$ colors in excess of 2.5 mag, indicating extinctions near or in excess of $A_V \simeq 40$. Of these, three (CS-010, 014, and 042) lie in the low extinction zone to the East of the cluster noted in Sect. 3.1 and excluded from our analysis of the cluster, and are probably distant luminous stars for which most of the foreground extincion is unrelated to the RCW 108 complex.

Of the remaining four, CSR-006 has a derived extinction of $A_V = 72$ mag which is in good agreement with the extinction produced by the molecular cloud on the foreground in that direction, as derived from the ^{13}CO maps presented in CSR05. However, Fig. 1 shows that the star lies precisely behind a narrow lane of dust that also obscures the nebula in that direction. It may thus be that the star is actually a cluster member, as supported by its also red ($K_S - L'$) color suggestive of infrared excess. CS-070 and CS-141 are both faint objects with rather uncertain H-band measurements that may have led to an overestimate of the extinction in their direction, especially in the case of CS-070 which is close to our threshold for the identification of possible background objects. Finally, CS-094 is also very red in ($K_S - L'$) and may actually be a low-mass object with substantial infrared excess, possibly also in the K_S-band. Since it is not detected at J we derived the extinction by assuming that the emission at K_S is photospheric (Sect. 3.3), which leads to an overestimate of the extinction if that assumption is incorrect. We can summarize our results regarding very red sources by stating that we find no strong evidence for any of these four objects being a background star, thus confirming that the dense column of molecular gas located behind the cluster provides an effective screen against such sources.

With only one exception, all the sources detected at L' are also seen in the K_S images. The exception is CS-109, a source well detected with $L' = 11.53$ projected outside the boundaries of the bright nebulosity to the North of CSR-012 subcluster. The darkness of the background in that region and the good adaptive optics correction that is attained so close to the wavefront sensing star, which is only 10″ away, allow us to set a very stringent limit of $K_S > 20.5$ at its position, implying $(K_S - L') > 9$. It is difficult to account for such extremely red color by assuming that CS-109 is a background star with normal colors obscured by the full column of dust in the molecular cloud. The necessary extinction is $A_V > 150$ mag, which is over twice that derived from the ^{13}CO maps but is not ruled out on small areas given the large beam size of the millimeter observations. However, the

Table 6. Very red objects detected at K_S.

Star	α(2000)	δ(2000)	K_S	$H-K_S$	K_S-L'	A_V
CSR-006	16:39:59.5	–48 51 56	14.019 ± 0.013	4.507 ± 0.079	3.728 ± 0.024	72.1
CS-010	16:40:02.8	–48 51 48	18.009 ± 0.050	3.058 ± 0.204	–	46.3
CS-014	16:40:02.7	–48 51 28	15.494 ± 0.010	3.543 ± 0.061	–	56.7
CS-042	16:40:02.1	–48 52 00	15.938 ± 0.026	2.511 ± 0.063	–	38.4
CS-070	16:40:01.2	–48 51 49	17.238 ± 0.088	2.676 ± 0.168	–	40.3
CS-094	16:40:00.3	–48 51 36	16.161 ± 0.025	2.993 ± 0.050	2.569 ± 0.100	47.7
CS-141	16:39:58.5	–48 51 54	16.984 ± 0.037	3.900 ± 0.291	–	62.3

Table 7. The candidate embedded protostar CS-109.

α(2000)	16:39:59.8
δ(2000)	–48:51:30
$f_{2.2\ \mu\mathrm{m}}$	<3 μJy
$f_{3.8\ \mu\mathrm{m}}$	(6.0 ± 0.2) mJy
$f_{4.5\ \mu\mathrm{m}}$	(18 ± 9) mJy
$f_{5.8\ \mu\mathrm{m}}$	(53 ± 32) mJy
$f_{8.0\ \mu\mathrm{m}}$	<123 mJy

absolute magnitude of an object reddened by such amount should be brighter than $M_{L'} = -7.9$. The limit assumes that the object is placed just behind the cloud at the distance of RCW 108, and that it is just below the detection limit in our K_S images. While all this is in principle possible (such an absolute magnitude could be attained by a bright Mira variable or a red supergiant), we deem the confluence of enumerated factors leading to its detection extremely unlikely.

An alternative possibility is that CS-109 is a protostellar object still deeply embedded in its parental core. To investigate it we have examined archive Spitzer images of the region obtained with the IRAC camera between 3.6 and 8.0 μm, which should help in extending or constraining the spectral energy distribution beyond the L' band. The object is faintly detected at 4.5 μm and marginally detected at 5.8 μm. The non-detection at 3.6 μm is in consistency with the flux measured in our L'-band images, and an upper limit is obtained at 8 μm. The measurement of fluxes in the two bands where the object is detected is made difficult by the steep brightness gradient of the nebulosity at its position, which prevents us from accurately determining the background emission level. Our measurements are listed in Table 7. CS-109 appears as a point source in our images despite their excellent resolution, implying the absence of extended structure with a linear size larger than about 70 AU.

Figure 9 shows the spectral energy distribution of this source. Despite the large uncertainty in the IRAC fluxes, it seems clear that the distribution rises towards longer wavelengths over the entire interval covered by our observations, consistent with it being a Class I or flat spectrum source, commonly interpreted as an embedded protostar (e.g. Adams et al. 1987). We must note however that it is unusual for Class I sources to be unresolved down to the scale probed by the L' observations (Whitney et al. 1997; Kenyon et al. 1998; Haisch et al. 2006). Deep diffraction-limited VLT observations in the 4–10 μm range should would be very valuable in confirming the true nature and spectral energy distribution of CS-109.

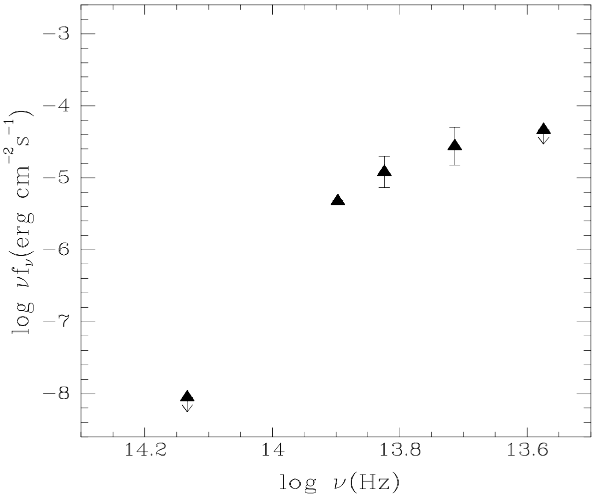

Fig. 9. Spectral energy distribution of the protostellar candidate CS-109.

4. Discussion

IRAS 16362-4845 is a relatively nearby example of the earliest evolutionary stages of a massive star forming cluster. Its youth is supported by its location embedded in the RCW 108 molecular cloud, the evidence for warm circumstellar material around a sizeable fraction of its members, the existence of one likely embedded protostar, and the fact that the HII region produced by the hottest stars of the cluster still has not excavated the surrounding molecular cloud beyond the boundaries of the cluster. However, perhaps the most important characteristic of the cluster is the possibility that it is an example of externally triggered star formation, for which additional tentative evidence in the region has been reported by Urquhart et al. (2004) and CSR05. It is thus interesting to discuss our findings in the light of this possibility.

The most intriguing feature of the IRAS 16362-4845 cluster found in the present study, which we have discussed at length in Sect. 3.5, is the unusually flat KLF. Translating the shape of the KLF to a shape of the IMF requires a number of assumptions (Muench et al. 2000), mainly about the age and star formation history of the cluster that are at present largely unknown. However, the flatness of the KLF strongly suggests a *top heavy* IMF with a deficit of low-mass stars. A second, and possibly related, unusual feature of the cluster is that, contrarily to what is observed in most clusters containing massive stars, the most massive members are not at the center. At near-infrared wavelengths the cluster is dominated by CSR-012A and its subgroup of companions, but several other bright stars for which we find similar or even brighter absolute magnitudes are scattered over the whole area of the cluster: most notably, CSR-006 and CSR-020 are candidate O-type stars based on their absolute magnitudes, in addition to CSR-012A, and are far removed from it.

The central location of the most massive stars in most clusters is thought to be of primordial nature due to their preferential formation at the bottom of the cluster potential well, rather than a result of dynamical evolution (Bonnell et al. 2007). This may play an important role in determining the shape of the IMF as a function of the distance to the cluster center in the competitive accretion scenario, leading to the preferential formation of low mass stars in the peripheral regions of the cluster. Low-mass stars might also be depleted at the centers due to coalescence to form more massive stars. We observe no hints of such mass segregation among the detected members of IRAS 16362-4845. Low-mass stars appear all across the cluster, but they do so in small numbers as implied by the shape of the K luminosity function (Fig. 8). Furthermore, it is obvious from Fig. 1 that the CSR-012 subcluster does not occupy a central position, but is rather located near the northern edge. The overall lack of low-mass stars might be interpreted in terms of competitive accretion as a result of the relatively widespread presence of massive stars, which would hamper the formation of low mass stars everywhere in the volume of the cluster rather than in the central regions only, contrarily to the more common case of clusters that have their most massive members at their centers.

Modern theoretical studies of the build-up of the IMF, based on the turbulent fragmentation and gravitational collapse of an isolated molecular cloud (see e.g. Bonnell et al. 2007, and references therein), have proven to be quite successful in reproducing both the shape of the IMF and the mass segregation evidences observed in many clusters. However, the mass spectrum resulting from externally triggered star formation might be markedly different from the one resulting from those studies, as noted by Zinnecker (1989), and remains largely unexplored. Indirect evidence for significant differences in the IMF resulting from triggered star formation, leading to the preferential formation of intermediate- and high-mass stars, has been reported (Sugitani et al. 1991; Dobashi et al. 2001; Getman et al. 2007). A recent study by Negueruela et al. (2007) of the young cluster NGC 1893, which contains both both early-type O stars and evidence for triggered star formation, also reports indications of a *top-heavy* IMF. Clearly, more modeling work is needed in order to obtain more quantitative predictions on the IMF resulting from triggered star formation (Elmegreen 2007). However, it may be noted that already the early modeling of the sequential star formation scenario by Elmegreen & Lada (1977) predicted the preferential formation of massive stars. The reasons for this are related to the warm temperature of the gas in the shocked layer located ahead of the ionization front produced by the triggering massive stars, to turbulence induced by Rayleigh-Taylor instabilities in this shocked layer, and to possible coalescence of unstable fragments in this layer. Observations like the ones reported here may provide the strongest constraints on future theoretical work.

5. Conclusions

The new observations of IRAS 16362-4845 presented in this paper represent a great improvement over previously existing ones, in terms of both depth and resolution, and give access to a more detailed study of its stellar population. The main conclusions of our work can be summarized as follows:

- The IRAS 16362-4845 cluster is embedded in a compact HII region that is ionization-bounded on its western side, where the density of the molecular cloud that harbors it is highest. The HII region appears to be open towards the East, in the direction towards the interface between the molecular cloud and the ionizing radiation of NGC 6193 that gives rise to the RCW 108 rim nebula.
- The stellar population of IRAS 16362-4845 is dominated by the small cluster around the star CSR-012, which is probably a late O-type star based on the results obtained by Comerón et al. (2005). Unlike in other clusters containing massive stars, CSR-012 is not centrally located but is actually displaced near the northern edge of the HII region. Other stars of similar brightness are seen throughout the cluster, but no concentration of bright stars with respect to the distribution of fainter ones is apparent.
- Earlier suspicions of an absence of low-mass stars in the IRAS 16362-4845 cluster are not confirmed by these new observations, which do detect a faint stellar component. Our observations sample the entire stellar mass range of IRAS 16362-4845 and reveal some likely brown dwarfs. Nevertheless, the numbers of low mass stars are well below the expectations drawn from the abundance of massive stars when a normal initial mass function is extrapolated to lower masses. We estimate that the cluster has a total stellar mass of $\sim 370\ M_\odot$.
- We estimate from the JHK_S photometry that most of the members of the IRAS 16362-4845 cluster have their K_S-band flux dominated by photospheric emission, with a contribution by circumstellar emission in that band that is either absent or moderate. Moreover, the vast majority of members display excess emission in the L' band.
- The K luminosity function of the cluster strongly suggests an atypical underlying initial mass function characterized by an overabundance of high mass stars. We are unable to identify any bias in our observations or our analysis that might possibly account for the shape of the K luminosity function if the initial mass function is normal.
- The diffraction-limited resolution of our L'-band observations allows us to identify 7 close (separation $<1''1$) binary or multiple systems, consistent with the multiplicity fractions in other massive star forming regions.
- IRAS 16362-4845 is still an active star forming site, as hinted by the existence of at least one extremely red object that is undetected below 3.8 μm. The rising spectrum up to at least 8 μm suggests that this is a Class I source.

At a distance of 1.3 kpc from the Sun, the stellar and even substellar content of IRAS 16362-4845 is both nearby and accessible to current instrumentation. Its location embedded in the core of a molecular cloud that is being photoevaporated by the stars of a nearby cluster raises the possibility that its formation may have been externally triggered. This makes it an attractive target to search for observational evidences of such a formation process. The main result of the present study is the derivation of a K luminosity function that suggests an overabundance of massive stars with respect to less massive ones. Together with the lack of a central concentration of massive stars, this might be such a signature of externally triggered star formation, as we speculate in this paper. Further theoretical modeling of the initial mass function produced in such scenario will be needed to assess whether or not this interpretation, which is tentative at the moment, is likely to be correct. Regardless of this, the new observations of IRAS 16362-4845 that we have presented here confirm it as an excellent example for the study of the properties of the youngest clusters containing massive stars.

Acknowledgements. We are pleased to acknowledge the advise of Dr. Lowell Tacconi-Garman at the ESO User Support Department in the preparation of our Service Mode observations. The Paranal Science Operations staff is warmly thanked for the careful execution of this program. We also thank Dr. Francesco Palla for making available to us the evolutionary tracks used in this paper, and Dr. Hans Zinnecker for useful comments on an early draft of this paper. The constructive comments of the referee, Dr. August Muench, helped improve the paper and are greatly appreciated.

References

Adams, F. C., Lada, C. J., & Shu, F. H. 1987, ApJ, 312, 788
Apai, D., Bik, A., Kaper, L., Henning, Th., & Zinnecker, H. 2007, ApJ, 655, 484
Arnal, E. M., May, J., & Romero, G. A. 2003, A&A, 412, 431
Bate, M. R., Bonnell, I. A., & Bromm, V. 2003, MNRAS, 336, 705
Baraffe, I., Chabrier, G., Allard, F., & Hauschildt, P. H. 2002, A&A, 382, 653
Baraffe, I., Chabrier, G., Barman, T. S., Al lard, F., & Hauschildt, P. H. 2003, A&A, 402, 701
Bertoldi, F. 1989, ApJ, 346, 735
Beuther, H., Churchwell, E. B., McKee, C. F., & Tan, J. C. 2007, in Protostars and Planets V, ed. B. Reipurth, D. Jewitt, & K. Keil (Univ. of Arizona Press)
Bonnell, I. A., Bate, M. R., & Zinnecker, H. 1998, MNRAS, 298, 93
Bonnell, I. A. 2005 [`arXiv:astro-ph/0501260`]
Bonnell, I. A., Larson, R. B., & Zinnecker, H. 2007, in Protostars and Planets V, ed. B. Reipurth, D. Jewitt, & K. Keil (Univ. of Arizona Press)
Bosch, G., Selman, F., Melnick, J., & Terlevich, R. 2001, A&A, 380, 137
Comerón, F., Schneider, N., & Russeil, D. 2005, A&A, 433, 955 (CSR05)
Dobashi, K., Yonekura, Y., Matsumoto, T., et al. 2001, PASJ, 53, 85
Duchêne, G., Simon, T., Eislöffel, J., & Bouvier, J. 2001, A&A, 379, 147
Elmegreen, B. G. 2007, in Massive Stars: from Pop III and GRBs to the Milky Way, ed. M. Livio, & E. Villaver (Cambridge Univ. Press)
Elmegreen, B. G., & Lada, C. J. 1977, ApJ, 214, 725
Figuerêdo, E., Blum, R. D., Damineli, A., & Conti, P. S. 2005, AJ, 129, 1523
Fujiyoshi, T., Smith, C., Moore, T. J. T., et al. 2005, MNRAS, 356, 801
García, B., & Mermilliod, J.-C. 2001, A&A, 368, 122
Garmany, C. D., Conti, P. S., & Massey, P. 1982, ApJ, 242, 1063
Getman, K. V., Feigelson, E. D., Garmire, G., Broos, P., & Wang, J. 2007, ApJ, 654, 316
Haisch, K. E., Barsony, M., Ressler, M. E., & Greene, T. P. 2006, AJ, 132, 2675
Kenyon, S. J., Brown, D. I., Tout, C. A., & Berlind, P. 1998, AJ, 115, 2491
Kroupa, P. 2001, MNRAS, 332, 231
Lada, C. J., & Adams, F. C. 1992, ApJ, 393, 278
Leistra, A., Cotera, A. S., & Liebert, J. 2006, AJ, 131, 2571
Lenzen, R., Hartung, M., Brandner, W., et al. 2003, SPIE, 4841, 944
Mason, B. D., Gies, D. R., Hartkopf, W. I., et al. 1998, AJ, 115, 821
Massi, F., Testi, L., & Vanzi, L. 2006, A&A, 448, 1007
Meyer, M. R., Calvet, N., & Hillenbrand, L. A. 1997, AJ, 114, 288
Miao, J., White, G. J., Nelson, R., Thompson, M., & Morgan, L. 2006, MNRAS, 369, 143.
Miller, G. E., & Scalo, J. M. 1979, ApJS, 41, 513
Muench, A. A., Lada, E. A., & Lada, C. J. 2000, ApJ, 533, 358
Muench, A. A., Lada, E. A., Lada, C. J., & Alves, J. 2002, ApJ, 573, 366
Muench, A. A., Lada, E. A., Lada, C. J., et al. 2003, AJ, 125, 2029
Negueruela, I., Marco, A., Israel, G., & Bernabeu, G. 2007, A&A, 471, 485
Palla, F., & Stahler, S. W. 1999, ApJ, 525, 772
Petersen, C. C. 2001, Sky & Telescope, 102, 54
Preibisch, T., Balega, Y., Hofman, K.-H., Weigelt, G., & Zinnecker, H. 1999, New Astron., 4, 531
Rieke, G. H., & Lebofsky, M. J. 1985, ApJ, 288, 618
Rousset, G., et al. 2002, SPIE, 4839, 140
Shaver, P. A., & Goss, W. M. 1970, Austr. J. Phys. Suppl., 14, 77
Skrutskie, M., Cutri, R. M., Stiening, R., et al. 2006, AJ, 131, 1163
Stetson, P. B. 1987, PASP, 99, 191
Straw, S., Hyland, A. R., Jones, T. J., et al. 1987, ApJ, 314, 283
Sugitani, K., & Ogura, K. 1994, ApJS, 92, 163
Sugitani, K., Fukui, Y., Mizuni, A., & Ohashi, N. 1989, ApJ, 342, L87
Sugitani, K., Fukui, Y., & Ogura, K. 1991, ApJS, 77, 59
Sugitani, K., Tamura, M., & Ogura, K. 1995, ApJ, 455, L39
Testi, L., Palla, F., & Natta, A. 1999, A&AS, 133, 81
Urquhart, J. S., Thompson, M. A., Morgan, L. K., & White, G. J. 2004, A&A, 428, 723
Whitney, B. A., Kenyon, S. J., & Gómez, M. 1997, ApJ, 485, 703
Wolk, S. J., Spitzbart, B. D., Bourke, T. L., et al. 2007, ApJ, submitted
Yorke, H. W., & Sonnhalter, C. 2002, ApJ, 569, 846
Zinnecker, H. 1989, in Evolutionary Phenomena in Galaxies, ed. J. E. Beckman, & B. E. J. Pagels (Cambridge Univ. Press)
Zinnecker, H., McCaughrean, M. J., & Wilking, B. A. 1993, in Protostars and Planets III (Univ. of Arizona Press)

Online Material

Table 2. Photometry of sources detected in the IRAS 16362-4845 cluster.

Name	RA(2000)	Dec(2000)	*J*	*H*	K_S	L'
CSR-001	16:39:58.3	–48:51:45	16.137 ± 0.008	14.124 ± 0.027	13.020 ± 0.005	11.872 ± 0.075
CSR-002	16:39:58.6	–48:52:05	13.948 ± 0.010	11.850 ± 0.010	10.568 ± 0.010	
CSR-003	16:39:58.7	–48:51:59		16.419 ± 0.019	14.471 ± 0.011	
CSR-004	16:39:59.0	–48:51:33	17.880 ± 0.007	14.815 ± 0.004	13.183 ± 0.008	10.611 ± 0.028
CSR-005A	16:39:59.5	–48:51:37	16.146 ± 0.010	12.823 ± 0.005	10.679 ± 0.008	7.878 ± 0.018
CSR-005B	16:39:59.5	–48:51:37	16.707 ± 0.011	13.781 ± 0.011	11.811 ± 0.016	9.822 ± 0.085
CSR-006	16:39:59.5	–48:51:56		18.526 ± 0.078	14.019 ± 0.013	10.291 ± 0.020
CSR-007	16:39:59.8	–48:51:59	15.867 ± 0.010	13.534 ± 0.015	12.250 ± 0.008	
CSR-008A	16:39:59.7	–48:51:39	13.127 ± 0.017	12.625 ± 0.022	12.324 ± 0.012	11.677 ± 0.039
CSR-008B	16:39:59.7	–48:51:39		16.135 ± 0.150	15.028 ± 0.150	11.017 ± 0.025
CSR-009A	16:39:59.9	–48:51:53	12.978 ± 0.004	12.040 ± 0.006	11.242 ± 0.006	10.807 ± 0.017
CSR-009B	16:39:59.9	–48:51:53				11.147 ± 0.044
CSR-010A	16:40:00.0	–48:51:42	14.478 ± 0.018	12.231 ± 0.010	10.662 ± 0.006	8.334 ± 0.021
CSR-010B	16:39:59.9	–48:51:42	18.874 ± 0.084	15.728 ± 0.081	13.985 ± 0.191	12.619 ± 0.076
CSR-010C	16:40:00.0	–48:51:42	18.836 ± 0.193	17.996 ± 0.049	16.315 ± 0.040	13.263 ± 0.056
CSR-011A	16:40:00.1	–48:51:45	17.502 ± 0.075	14.286 ± 0.034	12.894 ± 0.016	10.293 ± 0.015
CSR-011B	16:40:00.1	–48:51:45	15.598 ± 0.014	13.596 ± 0.029	12.607 ± 0.013	11.633 ± 0.030
CSR-012A	16:40:00.1	–48:51:40	10.872 ± 0.010	9.198 ± 0.010	8.356 ± 0.010	7.105 ± 0.025
CSR-012B	16:40:00.1	–48:51:40	14.187 ± 0.091	12.392 ± 0.040	10.897 ± 0.025	9.015 ± 0.023
CSR-012C	16:40:00.2	–48:51:39	14.651 ± 0.099	12.195 ± 0.053	10.953 ± 0.050	9.603 ± 0.020
CSR-012D	16:40:00.1	–48:51:41		12.981 ± 0.064	11.856 ± 0.050	9.981 ± 0.014
CSR-012E	16:40:00.2	–48:51:41	17.441 ± 0.113	14.571 ± 0.094	13.581 ± 0.099	12.628 ± 0.046
CSR-013	16:40:00.3	–48:51:59	13.101 ± 0.006	12.532 ± 0.024	12.335 ± 0.009	
CSR-014	16:40:00.3	–48:51:55	16.692 ± 0.022	14.796 ± 0.020	13.537 ± 0.008	12.658 ± 0.051
CSR-015	16:40:00.3	–48:51:46	16.679 ± 0.026	14.324 ± 0.033	13.008 ± 0.008	10.837 ± 0.022
CSR-016	16:40:00.3	–48:51:43	13.180 ± 0.013	11.148 ± 0.010	10.261 ± 0.005	8.924 ± 0.017
CSR-017	16:40:00.8	–48:51:38	16.019 ± 0.031	13.424 ± 0.029	11.769 ± 0.009	8.797 ± 0.024
CSR-018	16:40:01.2	–48:51:52	11.575 ± 0.010	10.255 ± 0.010	9.074 ± 0.010	5.510 ± 0.019
CSR-019A	16:40:01.3	–48:51:45	15.090 ± 0.004	12.845 ± 0.006	11.415 ± 0.008	10.113 ± 0.025
CSR-019B	16:40:01.2	–48:51:45				10.969 ± 0.045
CSR-020	16:40:01.6	–48:51:48	14.176 ± 0.010	11.294 ± 0.010	9.846 ± 0.007	7.142 ± 0.021
CSR-021	16:40:01.6	–48:51:41	20.054 ± 0.043	16.294 ± 0.024	14.377 ± 0.014	12.089 ± 0.046
CSR-022	16:40:01.7	–48:51:52	14.909 ± 0.009	13.105 ± 0.027	12.252 ± 0.007	11.204 ± 0.026
CSR-023	16:40:01.7	–48:51:38	17.642 ± 0.014	14.856 ± 0.021	13.362 ± 0.011	11.704 ± 0.044
CSR-024	16:40:01.9	–48:51:48	17.879 ± 0.020	15.030 ± 0.031	13.558 ± 0.010	12.814 ± 0.069
CSR-025	16:40:02.1	–48:51:55		15.289 ± 0.015	13.967 ± 0.009	
CS-001	16:40:03.0	–48:51:39		21.019 ± 0.235		
CS-002	16:40:03.0	–48:51:40		20.566 ± 0.194	19.496 ± 0.162	
CS-003	16:40:02.9	–48:51:47			18.038 ± 0.041	
CS-004	16:40:02.9	–48:51:49		20.925 ± 0.382	19.390 ± 0.077	
CS-005	16:40:02.9	–48:51:47			19.814 ± 0.267	
CS-006	16:40:02.8	–48:51:16			20.101 ± 0.283	
CS-007	16:40:02.9	–48:51:42			20.404 ± 0.227	
CS-008	16:40:02.8	–48:51:16			18.888 ± 0.156	
CS-009	16:40:02.8	–48:51:39		20.779 ± 0.188	18.705 ± 0.102	
CS-010	16:40:02.8	–48:51:48		21.067 ± 0.198	18.009 ± 0.050	
CS-011	16:40:02.8	–48:51:50		21.172 ± 0.195	19.101 ± 0.134	
CS-012	16:40:02.8	–48:51:53			19.335 ± 0.067	
CS-013	16:40:02.7	–48:51:52		20.263 ± 0.171	19.111 ± 0.103	
CS-014	16:40:02.7	–48:51:28		19.037 ± 0.060	15.494 ± 0.010	
CS-015	16:40:02.7	–48:51:47		19.945 ± 0.142	19.041 ± 0.082	
CS-016	16:40:02.6	–48:51:57			19.730 ± 0.167	
CS-017	16:40:02.6	–48:51:56			20.063 ± 0.122	
CS-018	16:40:02.6	–48:51:54			18.172 ± 0.066	
CS-019	16:40:02.6	–48:51:59		21.471 ± 0.300	20.420 ± 0.199	
CS-020	16:40:02.5	–48:51:50		20.298 ± 0.122	19.481 ± 0.080	
CS-021	16:40:02.5	–48:51:53		21.104 ± 0.131		
CS-022	16:40:02.5	–48:51:45		20.835 ± 0.137	19.491 ± 0.071	
CS-023	16:40:02.4	–48:51:30			19.618 ± 0.080	
CS-024	16:40:02.4	–48:51:15			20.611 ± 0.284	

Table 2. continued.

Name	RA(2000)	Dec(2000)	*J*	*H*	K_S	L'
CS-025	16:40:02.4	–48:51:43			20.531 ± 0.197	
CS-026	16:40:02.4	–48:51:43			19.624 ± 0.091	
CS-027	16:40:02.4	–48:51:49		20.485 ± 0.187	19.685 ± 0.143	
CS-028	16:40:02.4	–48:51:45		20.258 ± 0.120	18.676 ± 0.074	
CS-029	16:40:02.3	–48:51:36			17.236 ± 0.025	
CS-030	16:40:02.3	–48:51:42		20.805 ± 0.143	18.673 ± 0.058	
CS-031	16:40:02.3	–48:51:57		17.943 ± 0.032	15.511 ± 0.014	
CS-032	16:40:02.3	–48:51:48		20.546 ± 0.139	18.389 ± 0.087	
CS-033	16:40:02.3	–48:51:49		19.876 ± 0.090		
CS-034	16:40:02.3	–48:51:52		21.880 ± 0.290	21.407 ± 0.353	
CS-035	16:40:02.2	–48:51:51		17.962 ± 0.033	17.399 ± 0.035	
CS-036	16:40:02.2	–48:51:39		21.097 ± 0.207	19.327 ± 0.074	
CS-037	16:40:02.2	–48:51:51		19.981 ± 0.131	19.210 ± 0.122	
CS-038	16:40:02.2	–48:51:49		19.419 ± 0.090	17.698 ± 0.051	
CS-039	16:40:02.2	–48:52:02			18.601 ± 0.114	
CS-040	16:40:02.1	–48:51:43		21.136 ± 0.202	19.744 ± 0.126	
CS-041	16:40:02.1	–48:51:54		17.484 ± 0.097	15.787 ± 0.041	
CS-042	16:40:02.1	–48:52:00		18.449 ± 0.057	15.938 ± 0.026	
CS-043	16:40:02.1	–48:51:49		20.472 ± 0.156	19.602 ± 0.136	
CS-044	16:40:01.9	–48:51:48			17.681 ± 0.155	
CS-045	16:40:01.9	–48:51:53		16.855 ± 0.021	14.863 ± 0.013	
CS-046	16:40:01.9	–48:51:46		17.677 ± 0.043	16.543 ± 0.043	
CS-047	16:40:01.9	–48:51:43		19.772 ± 0.098	18.562 ± 0.060	
CS-048	16:40:01.9	–48:51:56			19.443 ± 0.093	
CS-049	16:40:01.8	–48:51:37	18.800 ± 0.028	14.950 ± 0.032	13.047 ± 0.009	10.912 ± 0.023
CS-050	16:40:01.8	–48:52:01	23.685 ± 0.734		18.944 ± 0.087	
CS-051	16:40:01.7	–48:51:45		21.594 ± 0.233	19.586 ± 0.343	
CS-052	16:40:01.8	–48:52:08			20.582 ± 0.270	
CS-053	16:40:01.6	–48:51:15			20.078 ± 0.159	
CS-054	16:40:01.7	–48:51:30			21.050 ± 0.289	
CS-055	16:40:01.7	–48:51:44		21.747 ± 0.294	19.757 ± 0.160	
CS-056	16:40:01.7	–48:51:58		19.437 ± 0.096	17.916 ± 0.074	
CS-057	16:40:01.5	–48:51:18	19.660 ± 0.032	18.460 ± 0.041	18.180 ± 0.038	
CS-058	16:40:01.6	–48:51:57	18.134 ± 0.020	16.503 ± 0.025	15.656 ± 0.021	
CS-059	16:40:01.5	–48:51:23			20.243 ± 0.143	
CS-060	16:40:01.4	–48:51:12			20.608 ± 0.262	
CS-061	16:40:01.5	–48:51:53		20.612 ± 0.138	18.976 ± 0.150	
CS-062	16:40:01.5	–48:51:32			20.467 ± 0.155	
CS-063	16:40:01.5	–48:52:06			18.418 ± 0.143	
CS-064	16:40:01.4	–48:51:33	19.206 ± 0.043	17.721 ± 0.045	16.752 ± 0.027	
CS-065	16:40:01.5	–48:52:09			19.990 ± 0.211	
CS-066	16:40:01.4	–48:51:54		16.900 ± 0.019	15.262 ± 0.020	
CS-067	16:40:01.3	–48:51:37			19.680 ± 0.162	
CS-068	16:40:01.3	–48:51:51		16.032 ± 0.070	14.317 ± 0.060	
CS-069	16:40:01.3	–48:51:47	17.326 ± 0.014	15.759 ± 0.033	15.134 ± 0.016	
CS-070	16:40:01.2	–48:51:49		19.914 ± 0.143	17.238 ± 0.088	
CS-071	16:40:01.1	–48:51:28			20.077 ± 0.286	
CS-072	16:40:01.1	–48:51:38		19.091 ± 0.099	17.195 ± 0.071	
CS-073	16:40:01.1	–48:51:50		17.333 ± 0.105	15.877 ± 0.111	
CS-074	16:40:01.1	–48:51:57			20.877 ± 0.287	
CS-075	16:40:01.0	–48:51:48		18.482 ± 0.055	17.172 ± 0.045	
CS-076	16:40:01.0	–48:51:39		18.328 ± 0.070	16.320 ± 0.116	
CS-077	16:40:00.9	–48:51:32	23.125 ± 0.269	21.380 ± 0.257		
CS-078	16:40:00.9	–48:51:49		20.756 ± 0.220	19.971 ± 0.162	
CS-079	16:40:00.9	–48:51:39		17.909 ± 0.131	18.101 ± 0.194	
CS-080	16:40:00.9	–48:51:42	20.131 ± 0.279			
CS-081	16:40:00.9	–48:51:48			19.137 ± 0.120	
CS-082	16:40:00.8	–48:51:46		21.096 ± 0.290	19.482 ± 0.398	
CS-083	16:40:00.8	–48:51:50		18.671 ± 0.084	16.370 ± 0.036	
CS-084	16:40:00.7	–48:51:39	19.891 ± 0.211	19.148 ± 0.165		
CS-085	16:40:00.7	–48:51:49		20.950 ± 0.193	19.718 ± 0.146	

Table 2. continued.

Name	RA(2000)	Dec(2000)	J	H	$K_{\rm S}$	L'
CS-086	16:40:00.6	–48:51:38			19.321 ± 0.176	
CS-087	16:40:00.7	–48:52:05	22.368 ± 0.282			
CS-088	16:40:00.6	–48:51:53	21.058 ± 0.196			
CS-089	16:40:00.6	–48:51:44		17.756 ± 0.108	17.210 ± 0.099	
CS-090	16:40:00.5	–48:51:40	20.451 ± 0.193			
CS-091	16:40:00.4	–48:51:40		16.088 ± 0.037	14.594 ± 0.013	11.597 ± 0.028
CS-092	16:40:00.4	–48:51:38			19.199 ± 0.244	
CS-093	16:40:00.4	–48:51:42	19.382 ± 0.187	16.014 ± 0.176	14.341 ± 0.088	12.003 ± 0.030
CS-094	16:40:00.3	–48:51:36		19.154 ± 0.043	16.161 ± 0.025	13.592 ± 0.097
CS-095	16:40:00.3	–48:51:29			19.196 ± 0.197	
CS-096	16:40:00.3	–48:51:56	17.340 ± 0.026	16.388 ± 0.057	15.777 ± 0.114	
CS-097	16:40:00.3	–48:51:51	17.944 ± 0.047	15.746 ± 0.030	14.388 ± 0.018	12.598 ± 0.056
CS-098	16:40:00.3	–48:52:03			18.704 ± 0.172	
CS-099	16:40:00.2	–48:51:37	21.618 ± 0.073	19.352 ± 0.027	16.990 ± 0.019	14.118 ± 0.087
CS-100	16:40:00.0	–48:51:37	20.749 ± 0.275			
CS-101	16:40:00.1	–48:52:05		20.458 ± 0.148		
CS-102	16:40:00.0	–48:52:02	19.980 ± 0.042	16.720 ± 0.027	15.294 ± 0.022	
CS-103	16:40:00.0	–48:51:38	18.609 ± 0.133	15.795 ± 0.091	13.959 ± 0.041	10.850 ± 0.017
CS-104	16:40:00.0	–48:51:40		15.241 ± 0.059	14.438 ± 0.050	11.934 ± 0.040
CS-105	16:39:59.9	–48:51:34			18.564 ± 0.232	
CS-106	16:39:59.9	–48:51:48		19.068 ± 0.149	18.449 ± 0.174	
CS-107	16:40:00.0	–48:52:01	21.226 ± 0.103	17.405 ± 0.036	15.632 ± 0.012	
CS-108	16:39:59.9	–48:52:10			20.758 ± 0.264	
CS-109	16:39:59.8	–48:51:30				11.532 ± 0.026
CS-110	16:39:59.8	–48:51:29			20.136 ± 0.214	
CS-111	16:39:59.8	–48:51:41			18.994 ± 0.269	
CS-112	16:39:59.7	–48:51:34			18.761 ± 0.254	
CS-113	16:39:59.8	–48:51:58	17.791 ± 0.022	14.694 ± 0.027	13.105 ± 0.009	11.207 ± 0.031
CS-114	16:39:59.7	–48:52:01			19.229 ± 0.211	
CS-115	16:39:59.7	–48:51:40	20.867 ± 0.580	18.804 ± 0.227		
CS-116	16:39:59.7	–48:52:07			20.042 ± 0.299	
CS-117	16:39:59.6	–48:51:52	20.961 ± 0.145		20.035 ± 0.211	
CS-118	16:39:59.5	–48:51:53		21.138 ± 0.480	18.750 ± 0.168	
CS-119	16:39:59.5	–48:51:45			19.662 ± 0.295	
CS-120	16:39:59.4	–48:51:39			19.513 ± 0.197	
CS-121	16:39:59.4	–48:51:29		21.678 ± 0.203		
CS-122	16:39:59.4	–48:51:48			19.261 ± 0.144	
CS-123	16:39:59.4	–48:52:07			20.298 ± 0.259	
CS-124	16:39:59.4	–48:51:49		20.071 ± 0.144	18.473 ± 0.111	
CS-125	16:39:59.3	–48:51:38		21.810 ± 0.296	19.480 ± 0.387	
CS-126	16:39:59.3	–48:51:28			18.968 ± 0.093	
CS-127	16:39:59.3	–48:51:42			18.955 ± 0.269	
CS-128	16:39:59.3	–48:51:37		16.544 ± 0.019	14.886 ± 0.015	12.059 ± 0.054
CS-129	16:39:59.3	–48:51:52			19.307 ± 0.097	
CS-130	16:39:59.2	–48:51:37	20.904 ± 0.133	18.634 ± 0.110		
CS-131	16:39:59.2	–48:51:42			18.623 ± 0.162	
CS-132	16:39:59.1	–48:51:58			20.445 ± 0.218	
CS-133	16:39:59.1	–48:52:03		17.353 ± 0.029	15.573 ± 0.015	
CS-134	16:39:59.0	–48:51:55			19.664 ± 0.191	
CS-135	16:39:58.9	–48:51:40			18.340 ± 0.138	
CS-136	16:39:58.9	–48:51:38			18.304 ± 0.160	
CS-137	16:39:58.9	–48:51:59		20.466 ± 0.200	18.377 ± 0.090	
CS-138	16:39:58.8	–48:51:17		19.997 ± 0.126	17.362 ± 0.025	
CS-139	16:39:58.8	–48:51:45	15.889 ± 0.011	15.074 ± 0.024	15.207 ± 0.019	
CS-140	16:39:58.8	–48:51:30		22.202 ± 0.281		
CS-141	16:39:58.5	–48:51:54		20.884 ± 0.289	16.984 ± 0.037	
CS-142	16:39:58.4	–48:51:55			20.810 ± 0.264	
CS-143	16:39:58.2	–48:51:43	20.997 ± 0.167			
CS-144	16:39:58.1	–48:51:28		17.934 ± 0.041	15.933 ± 0.015	
CS-145	16:39:58.0	–48:51:47	19.548 ± 0.047	18.165 ± 0.051	17.328 ± 0.045	
CS-146	16:39:58.0	–48:52:09		21.321 ± 0.251		
CS-147	16:39:57.9	–48:51:43		15.976 ± 0.026	15.159 ± 0.009	